

SUMMARY REPORT OF CHLORINE-36 STUDIES:

**SYSTEMATIC SAMPLING FOR CHLORINE-36
IN THE EXPLORATORY STUDIES FACILITY**

by

**J.T. Fabryka-Martin, P.R. Dixon, S. Levy, B. Liu, H.J. Turin,
and A.V. Wolfsberg**

Los Alamos National Laboratory

Abstract

In order to assess groundwater travel times and to identify potential fast paths for infiltrating water, the distribution of chlorine-36 (^{36}Cl) in the ESF tunnel has been determined from analyses of samples collected at 52 locations between Stations 2 and 36. Rock samples were collected systematically every 200 m throughout the tunnel as well as from diverse geologic features such as faults, fractures, and lithophysal cavities. All of the systematic samples as well as most of the feature-based samples contain ^{36}Cl levels consistent with travel times exceeding a few thousand years. Upper age limits range up to several hundred thousand years. Uncertainties about temporal variations in the atmospheric $^{36}\text{Cl}/\text{Cl}$ input ratio prevent calculation of more precise ground-water travel times at this time. Bomb-pulse ^{36}Cl occurs at a few distinct fractured and/or faulted zones, indicating that at least a small proportion of the water at these locations is less than 50 years old.

A flow and transport model using the FEHM code is used to simulate transport of ^{36}Cl into the ESF tunnel. Modeling results show that observed ^{36}Cl signals are consistent with existing site conceptual models and parameter estimates. Base-case parameters predict Pleistocene-aged water in the ESF, while parameter changes consistent with increased fracturing of the PTn unit (as might be associated with faults) lead to a prediction of a small component of bomb-pulse ^{36}Cl in ESF fractures. Thus, these modeling results show that the new ^{36}Cl data presented in this report do not require a major re-evaluation of previous work.

The data presented were developed under YMP quality assurance (QA) procedures and have been technically reviewed. The formal technical review required by the LANL/YMP QA program will be completed prior to publication of the data in a Level 3 milestone report due in August 1996.

Contents

	Page
List of Tables	iii
List of Figures	iii
1. Objectives of Sampling in the Exploratory Studies Facility (ESF)	1
2. Sample Collection Protocol	2
3. Sample Descriptions	3
4. Analytical Results	4
4.1 Sample Processing	4
4.2 Cl and Br Analyses of ESF Construction Water	4
4.3 Analytical Results for ESF Rock Samples	5
5. Preliminary Interpretations of ESF Data	6
5.1 Reconstruction of Past Meteoric ³⁶ Cl/Cl Signal	6
5.2 Alternative Interpretations of ³⁶ Cl/Cl Signals in ESF Samples	7
5.3 Evidence for Controls of Water Movement	8
5.4 Comparison of ³⁶ Cl Results for ESF and Borehole Samples	9
6. Flow and Transport Model	10
6.1 Introduction	10
6.2 Modeling Approach	11
6.3 Base Case Results	13
6.4 Effects of PTn Parameters on Rapid Transport	14
6.5 Modeling Limitations	18
6.6 Discussion of Modeling Effort	20
7. Conclusions	21
8. Suggestions for Future Work	21
Acknowledgments	22
References	23
Appendix A. Site and Sample Descriptions	A-1

List of Tables

	Page
1. ESF samples collected for ^{36}Cl analysis, November 1995 to February 1996	25
2. PTn samples marked for collection as of 9-February-1996	30
3. Summary of samples collected, by feature	31
4. Analyses of J#13 well water and ESF construction water	32
5. Measured $^{36}\text{Cl}/\text{Cl}$ ratios in ESF samples, sorted by station	33
6. Correction of measured $^{36}\text{Cl}/\text{Cl}$ ratios for dilution by rock chloride, for ream-cutting samples from borehole UE-25 UZ#16	37
7. Correction of measured $^{36}\text{Cl}/\text{Cl}$ ratios for dilution by rock chloride, for ream-cutting samples from borehole USW UZ-14	39
8. PTn fracture parameters for FEHM simulations	40
9. Travel-time estimates (years) from FEHM simulations	41

List of Figures

1. Schematic plan view of ESF North Ramp, Main Drift, and South Ramp projections, showing locations of major faults and nearby boreholes for which samples exist for chlorine-36 analysis	42
2. Schematic cross-section of ESF tunnel, showing approximate locations of the surface, major stratigraphic units, and major structural features as a function of distance along the North Ramp and Main Drift	43
3. Distribution of $^{36}\text{Cl}/\text{Cl}$ ratios measured for rock samples, as a function of distance along the ESF North Ramp and Main Drift	44
4. Variations in geomagnetic field intensity and corresponding theoretical production of chlorine-36 in the atmosphere	45
5. Predicted variations in production of chlorine-36 in the atmosphere, compared against measured data for packrat middens and alluvial porewaters from the vicinity of the Nevada Test Site	46

List of Figures (continued)

	Page
6. Upper limits for ground water travel times as a function of distance along the ESF North Ramp and Main Drift	47
7. Frequency distribution of upper limits for ground water travel times in the ESF, assuming a maximum initial meteoric $^{36}\text{Cl}/\text{Cl}$ ratio of 1500 ($\times 10^{-15}$)	48
8. Station 35 description and model results for base-case properties and 1 mm/yr infiltration rate	49
9. Cumulative breakthrough at ESF for 1.0 mm/yr and base-case properties	50
10. Cumulative breakthrough at ESF for 0.1 mm/yr and base-case properties	50
11. Cumulative breakthrough at ESF for 5.0 mm/yr and base-case properties	51
12. Cumulative breakthrough at ESF for 5.0 mm/yr and Case A properties	51
13. Cumulative breakthrough at ESF for 5.0 mm/yr and Case B properties	52
14. Cumulative breakthrough at ESF for 5.0 mm/yr and Case C properties	52
15. Cumulative breakthrough at ESF for 5.0 mm/yr and Case D properties	53
16. Cumulative breakthrough at ESF for 5.0 mm/yr and Case E properties	53

**SUMMARY REPORT OF CHLORINE-36 STUDIES:
SYSTEMATIC SAMPLING FOR CHLORINE-36
IN THE EXPLORATORY STUDIES FACILITY**

1. Objectives of Sampling in the Exploratory Studies Facility (ESF)

A testable conceptual model for water movement in the unsaturated zone at Yucca Mountain includes several key hypotheses:

- ▶ the Paintbrush nonwelded (PTn) unit is an effective barrier to vertical flow;
- ▶ water in the matrix of the Topopah Spring welded (TSw) unit is essentially stagnant; and
- ▶ water that reaches the Calico Hills nonwelded (CHn) unit or accumulates in perched water bodies for the most part arrives at these locations via a few isolated fast paths and is thereafter redistributed laterally in the matrix along permeability boundaries.

To some extent, the validity of these hypotheses can be evaluated through systematic sampling and analysis of rocks in the ESF tunnel and its alcoves, for hydrologic, geochemical, isotopic, and mineralogic characteristics in combination with hydrologic and solute transport modeling. LANL began a comprehensive sampling of rocks in the ESF in November 1995 to identify preferential flow paths and to estimate residence times for groundwater throughout this facility based upon measurements of chloride (Cl), bromide (Br) and chlorine-36 (^{36}Cl) concentrations in the rock porewaters. This radioactive isotope is produced in the atmosphere and carried underground with percolating groundwater. Where the residence time of water is of the same order of magnitude as the ^{36}Cl half-life (301 ky), this age may be estimated by the extent of decay of the meteoric ^{36}Cl . High concentrations of this isotope were also added to meteoric water during a period of global fallout from atmospheric testing of nuclear devices, primarily in the 1950s. This bomb-pulse signal can be used to test for the presence of fast transport paths.

A parallel ESF study was started at the same time by the U.S. Geological Survey (USGS), using the extent of disequilibrium in uranium (U) and thorium (Th) activity ratios to estimate deposition ages of fracture and cavity mineral coatings, as a surrogate indicator of past groundwater flow through these features. Preliminary results for that effort were reported in Paces (1996).

2. Sample Collection Protocol

Figure 1 presents a plan view of the ESF tunnel with the approximate locations of major faults and nearby boreholes for which samples are available for ^{36}Cl analysis. The schematic cross-section in Figure 2 shows elevations of the surface, major stratigraphic units, and major faults

from the North Portal entrance at Station 0 to Station 40. Depths beneath the surface for this portion of the ESF range from 50 to 280 m, with depths generally increasing with distance.

The sampling plan for the LANL activity contains both systematic as well as feature-based criteria, targeting three general types of sampling locations in the tunnel:

- ▶ systematic sampling of bulk rock material every 200 m through the TSw and PTn units,
- ▶ sampling of potential fast paths throughout the ESF, focussing particularly on the TSw unit, and
- ▶ sampling at selected stratigraphic contacts in the PTn unit to evaluate their influence on diverting vertical water movement.

Sample sites in this report were selected during five joint field trips with USGS personnel involved in related studies. Initial field and laboratory activities have focussed on the potential repository horizon. All samples for the LANL effort are collected using a dry chipping or drilling technique. Typical sample sizes range from 1 to 20 kg to ensure sufficient material for isotopic analysis.

An early concern regarding samples collected from the tunnel walls was the possible presence of construction water that could modify the natural porewater chemistry and give a ^{36}Cl signal that was not representative of natural conditions. Construction water, which contains lithium bromide (LiBr) tracer, is used for several operations in the ESF that could result in the presence of this traced water in samples collected from tunnel walls. These uses include the Tunnel Boring Machine (TBM) cutter head, wet-drilling for installation of rock bolts, dust control on the muck belt, and spraying the tunnel ribs to facilitate fracture mapping. To minimize the contribution of Cl from construction water, samples intended for bulk analysis are collected after the outermost 10 cm of rock are removed. Br/Cl analyses are used to evaluate the extent to which Cl derived from the construction water may be present in a given sample (section 4.3).

Table 1 lists 89 ESF rock samples collected specifically for this effort between November 29, 1995, and February 9, 1996, plus 10 of the rock samples collected previously by the U.S. Bureau of Reclamation (BuRec) as part of the YMP Program for Consolidated Sampling in the ESF. Systematic sampling of the tunnel every 200 m from Stations 5 to 39 produced 18 samples (excluding one marked at Station 31 which could not be collected due to inaccessibility). The remaining samples were collected from a variety of geologic features: broken rock, breccia, open and closed fractures, shear zones, cooling joints, fault zones, lithophysal cavities, and stratigraphic contacts. In many cases, secondary mineral deposits—predominantly calcite and opal—were removed from the bedrock at these locations. The primary objective was to collect samples from a variety of structural features to allow testing of conceptual models of flow and transport into the ESF. To the extent possible, samples were collected to correspond with USGS samples for U-Th analysis and facilitate comparison between groundwater travel times based on ^{36}Cl analyses and mineral deposition ages obtained from U-Th isotopic analyses.

Altogether, 29 sampling locations at 13 different stations were marked in the ESF where the PTn is exposed between Stations 5 and 11 and in Alcoves 3 and 4 (Table 2). As of February 28,

1996, 12 samples had been collected from this part of the ESF but none had been analyzed because the maximum effort has been applied to TSw samples. The sites were selected in close consultation with USGS scientists, mostly to investigate the possible role of stratigraphic contacts within the PTn in diverting downward flow away from the TSw.

3. Sample Descriptions

Table 1 briefly describes the presence of structural features and secondary mineral deposits for each of the collected samples. Table 3 summarizes the samples collected by type of feature. The majority of samples collected in the ESF are associated with discrete rock features that may be considered at least potential flow paths. Nearly 60% of the samples are from faults or fractures, 10% are from lithophysal cavities, 10% are from unit contacts, and the remaining 20% are part of the systematic sampling effort.

One of the goals of the present activity is to identify any associations between the nature of the potential pathway and the evidence of flow based on ^{36}Cl data. Sampled features can be classified as either syngenetic (formed while the host tuff was cooling) or tectonic (formed in response to regional stresses), although the two categories need not be mutually exclusive. This classification scheme was selected because the two categories can be expected to differ in the likelihood of providing a flow path that is continuous across units or that extends to the surface. Syngenetic features such as cooling joints, lithophysal cavities and their interconnecting fracture systems, and some breccia zones, formed while the host tuff was cooling and do not extend upward into overlying, younger lithologic units. Mineralogic evidence often exists that links these features to the early cooling history of the host rock. Lithophysal cavities (also called lithophysae) are relict gas cavities also of syngenetic origin and are commonly linked by networks of fractures. In contrast, tectonic features such as faults (defined as a feature for which there is evidence of wall-rock offset), some breccia zones, and some fractures, formed in response to long-lived regional stress patterns, can cross stratigraphic boundaries, and may extend upward to the ground surface. As noted above, the two categories need not be mutually exclusive because syngenetic features can be modified by later tectonic activity. Fault offset along an existing cooling joint is an example of such hybrid origin.

The genesis of a particular structural feature was not always evident from preliminary field work. Individual fractures of unknown or ambiguous origin are referred to simply as "fractures" in Table 1, and the same is true for fracture zones. The origins of some fractures and fracture zones—for example, their probable association with low-offset fault zones—may be inferred in the future from fracture maps produced by the BuRec when these are completed. Broken rock, breccia, and rubble are additional examples of non-genetic terms.

Detailed descriptions of the sampling locations are provided in Appendix A to document the nature of the bedrock, the presence of field-scale structures such as faults, fractures, breccia zones, lithophysal cavities and other features that may affect rock permeability, and the existence of secondary mineral deposits indicating the past movement of water through the rocks. The

descriptive process is in progress and many of the descriptions still lack either site or sample information.

4. Analytical Results

4.1 Sample Processing

Chloride is extracted from samples for isotopic analysis by leaching the material with an equal mass of deionized water for 48 hours. Typical sample sizes are 1 to 5 kg of rock. In most cases, the Cl of interest is on the outer surfaces of particles, representing porewater. Unconsolidated or poorly consolidated material such as fault gouge is leached in the same form as it is received. For most other samples, the rock must first be crushed with a hammer to create chips of dimensions approximately 3-4 cm prior to leaching. At the end of the 48-hour period, an aliquot of the leachate is removed for Cl and Br analysis by ion chromatography. These analyses are used to assess the extent to which Cl from construction water may be present in the sample (section 4.3). The remainder of the leachate is decanted and acidified to promote settling of fine particulates, then filtered. If the quantity of Cl in a sample is insufficient for analysis, it is augmented by the addition of a known quantity of isotopically pure chlorine-35 (^{35}Cl), a standard analytical technique called isotope dilution. Silver nitrate is added to the leachate to precipitate silver chloride (AgCl). The AgCl is subsequently purified of sulfur impurities by multiple cycles of dissolution in ammonium hydroxide, addition of barium nitrate to precipitate barium sulfate, followed by reprecipitation of the AgCl with nitric acid. AgCl precipitates are sent to the Purdue Rare Isotope Measurement Laboratory at Purdue University for Cl isotope analysis by accelerator mass spectrometry.

4.2 Cl and Br Analyses of ESF Construction Water

ESF construction water was sampled from lines throughout the tunnel in order to provide data needed to evaluate the extent to which this source could be contributing Cl to the rock samples. Water samples were collected by the Test Coordination Office (TCO) from various locations including the mixing tank where the LiBr tracer is added, several points of use within the ESF, and the return flow from the ESF. Halide and $^{36}\text{Cl}/\text{Cl}$ analyses of these samples and of well J#13 source water are reported in Table 4. These data confirm that the construction water is being traced, with appropriate precision and accuracy, to a Br concentration of 20 ± 2 mg/L. However, this very limited data set also suggests that Cl concentrations may vary significantly over time, with corresponding variation in the Br/Cl ratio, which is the parameter most relevant to the ^{36}Cl activity.

Increased Cl concentrations in the used water, as much as 4 times the concentration in the original water, presumably result from a combination of evaporation and addition of salts released from the rock during drilling. Br concentrations increase to a lesser extent. Because of the negligibly low concentration of Br in the rock, increases in Br concentrations in the traced water after use should reflect the effects of evaporation only, provided there is no contribution

from unintended sources of contamination. The TCO is continuing sample collection as part of this activity, in order to monitor halide concentrations in the construction water.

4.3 Analytical Results for ESF Rock Samples

Table 5 summarizes the 52 isotopic and halide analyses available to-date. Measured $^{36}\text{Cl}/\text{Cl}$ ratios reported in this table have been corrected for any addition of ^{35}Cl tracer. The measured ratios are then adjusted for the presence of Cl from construction water as described below. The final reported uncertainty includes propagation of analytical uncertainties from the reported $^{36}\text{Cl}/\text{Cl}$ and Br/Cl measurements. Final corrected ratios with uncertainties exceeding 25% have been omitted from Table 5.

As mentioned previously, the possible presence of construction water in the rock samples is evaluated through the analysis of Br/Cl ratios. The Br/Cl ratio for construction water is between 2 and 3 (Table 4, section 4.2 above) due to the addition of LiBr tracer, while the ratio for percolating water is estimated to be about 0.009 ± 0.002 (Fabryka-Martin and Liu, in prep.). For comparison, the Br/Cl ratio for halides from fluid inclusions in the rock is even lower, about 0.002. Thus, high Br/Cl ratios of some of the ESF samples indicate the presence of a small proportion of Cl derived from the traced construction water. The proportion of Cl contributed by construction water (f_c) can be estimated from the measured Br/Cl (halide) ratio, HR_x , using a two-component mixing equation:

$$f_c = (\text{HR}_x - \text{HR}_m) / (\text{HR}_c - \text{HR}_m) \quad (1)$$

where HR_m is the Br/Cl ratio of meteoric water (0.009) and HR_c is the Br/Cl ratio of construction water (3.0). Based on these values and equation (1), a sample with a measured ratio of 0.5 would derive about 16% of its Cl from construction water. The result is only a crude estimate because the end-member values are somewhat variable and because the contribution of halides released from rock fluid inclusions is not included in the simplistic two-component mixing model. The release of halides appears to be negligible, at least for poorly consolidated material such as gouge, based on the results of experiments in which a sample is repeatedly crushed and leached.

In general, the presence of construction water in the samples does not appear to pose a problem for the reliability of the isotopic results. The contribution of Cl from construction water appears to be <10% (i.e., Br/Cl ratios ≤ 0.4) of the total Cl of the sample in most cases listed in Table 5. Measured $^{36}\text{Cl}/\text{Cl}$ ratios (R_x) in Table 5 have been adjusted for the presence of construction water to obtain corrected meteoric $^{36}\text{Cl}/\text{Cl}$ ratios, R_m , using the following equation:

$$R_m = (R_x - f_c R_c) / (1 - f_c) \quad (2)$$

in which R_c is the $^{36}\text{Cl}/\text{Cl}$ ratio of the construction water, $500 (x 10^{-15})$. It is important to note that, based on $^{36}\text{Cl}/\text{Cl}$ analyses of the construction water, Cl from this source would generally

dilute—not increase—the measured $^{36}\text{Cl}/\text{Cl}$ signal in a sample. Thus, ^{36}Cl levels above present-day background cannot be attributed to this source.

Figure 3 plots $^{36}\text{Cl}/\text{Cl}$ results from Table 5 as a function of distance into the ESF tunnel. The data fall clearly into two distinct populations. All of the systematic samples and most of the feature-based ones have corrected $^{36}\text{Cl}/\text{Cl}$ ratios ranging from 400 ($\times 10^{-15}$) to 1300 ($\times 10^{-15}$), or 0.8 to 2.6 times the present-day background-value of 500 ($\times 10^{-15}$) (Fabryka-Martin et al., 1993). At a few locations, such as the Bow Ridge Fault zone, ratios extend well above this range, to a maximum of 3800 ($\times 10^{-15}$).

5. Preliminary Interpretations of ESF Data

5.1 Reconstruction of Past Meteoric $^{36}\text{Cl}/\text{Cl}$ Signal

In order to estimate the travel time of ground water in the ESF samples, temporal variations in the input value of atmospheric $^{36}\text{Cl}/\text{Cl}$ must be known. A value of 500 ($\times 10^{-15}$) was used in previous reports as an initial value for estimating groundwater travel time in the unsaturated zone of Yucca Mountain (Fabryka-Martin et al., 1993). However, the atmospheric $^{36}\text{Cl}/\text{Cl}$ value has not been constant over time, as indicated by a small but convincing set of evidence (e.g., Plummer, 1996; Tyler et al., in press) as well as theoretical modeling of atmospheric physics.

The meteoric $^{36}\text{Cl}/\text{Cl}$ ratio is a result of two variable processes: cosmogenic production rate of ^{36}Cl in the atmosphere, and wet and dry deposition rates of stable Cl. Production of ^{36}Cl in the atmosphere is a function of atmospheric cosmic-ray intensity, which is in turn controlled by temporal variations in the earth's geomagnetic field intensity (Mazaud et al., 1991). The ^{36}Cl production rate is high when the geomagnetic field intensity is low, and vice versa. Based on reconstructions of the paleomagnetic field intensity, ^{36}Cl production was considerably higher than its present rate for much of the past 500 ky, possibly on the order of twice its present value (Figure 4) (using data of Tric et al., 1992; and Valet and Meynadier, 1993, based on the approach of Mazaud et al., 1991).

Variations in the stable Cl deposition rate are more difficult to reconstruct. These variations are a product of changing meteorologic patterns over the western U.S., and changing source regions, such as salt flats and presently dry lake beds. Bounding estimates of these variations will be made in the future; for now, discussion in this paper is based on the assumption that the Cl deposition rate has varied $\pm 25\%$ relative to its present rate of 106 mg Cl/m²/yr (Fabryka-Martin et al., 1993).

Assuming a constant Cl deposition rate, the value of the atmospheric $^{36}\text{Cl}/\text{Cl}$ ratio at Yucca Mountain during the past 500 ky could have been as high as 1100 ($\times 10^{-15}$), slightly more than twice its present value of 500 ($\times 10^{-15}$), and as low as 420 ($\times 10^{-15}$) (Figure 4). A Cl deposition rate 75% of the modern rate would yield a maximum meteoric $^{36}\text{Cl}/\text{Cl}$ ratio of 1470 ($\times 10^{-15}$). This peak in the signal would have occurred about 40 ky ago. The $^{36}\text{Cl}/\text{Cl}$ ratio has been

measured in packrat middens (this work) collected from the Yucca Mountain area and dated by the ^{14}C method, and in pore water from a deep borehole penetrating alluvium at Area 5 of the Nevada Test Site (Tyler et al., in press). Both data sets confirm the model reconstruction of higher atmospheric $^{36}\text{Cl}/\text{Cl}$ ratios at Yucca Mountain at least over the past 50 ky (Figure 5). On this figure, the packrat midden data agree fairly well with the reconstructed meteoric $^{36}\text{Cl}/\text{Cl}$ signal based on the lower Cl deposition rate. A direct comparison of the data of Tyler et al. (in press) with the predicted $^{36}\text{Cl}/\text{Cl}$ signal is not as straightforward because a constant Cl deposition rate was assumed in estimating the sample ages from the accumulation of Cl in the alluvial profile. Decreasing the assumed Cl deposition rate causes a proportional increase in the ages corresponding to the borehole $^{36}\text{Cl}/\text{Cl}$ data, whereas an increased rate causes a decrease in the ages, as indicated by the range of ages shown for the alluvial samples in Figure 5.

5.2 Alternative Interpretations of $^{36}\text{Cl}/\text{Cl}$ Signals in ESF Samples

An important conclusion to be drawn from the packrat and alluvial porewater data as well as from theoretical calculations of ^{36}Cl production rates is that a constant initial $^{36}\text{Cl}/\text{Cl}$ ratio of 500 ($\times 10^{-15}$) should not be used to estimate groundwater travel time at Yucca Mountain, and that the initial ratio could have been two to three times higher during the past several hundred thousand years. As a result, only sample $^{36}\text{Cl}/\text{Cl}$ ratios significantly higher than 1500 ($\times 10^{-15}$) are interpreted as clear bomb-pulse ^{36}Cl signals (Table 5, last column); samples with ratios ≤ 1500 ($\times 10^{-15}$) may contain a component of bomb-pulse ^{36}Cl but may also contain Cl from old waters recharged when the input ratio was higher. Bomb-pulse signals clearly occur in samples from a few fault zones, fractures, and shear zones, implying that these individual features are active paths for preferential flow.

In contrast, none of the systematic samples nor most of the feature-based samples have $^{36}\text{Cl}/\text{Cl}$ values greater than 1300 ($\times 10^{-15}$) (Table 5). For these samples, three alternative scenarios are proposed to explain the measured $^{36}\text{Cl}/\text{Cl}$ results on the basis of different initial $^{36}\text{Cl}/\text{Cl}$ ratios for the percolating water.

Scenario 1: Modern water. According to this scenario, travel times for water in the ESF are assumed to be sufficiently fast that an initial ratio of 500 ($\times 10^{-15}$) can be assumed. Water in the collected samples is assumed to represent a mixture of water parcels, each having different travel times as a result of traveling along different flow paths, and hence may include variable fractions of water containing bomb-pulse ^{36}Cl . Samples having $^{36}\text{Cl}/\text{Cl}$ ratios higher than 500 ($\times 10^{-15}$) indicate at least a small component of bomb-pulse water is present. Essentially, a bomb-pulse ^{36}Cl signal exists everywhere by this scenario.

This first scenario is highly improbable because it is inconsistent with the measured distributions of bomb-pulse tritium and ^{14}C in YMP boreholes, which indicate that such fast paths, while present, do not appear to be a widespread phenomenon at this site.

Scenario 2: Travel times ≤ 50 ky (Holocene to late Pleistocene water). Although a bomb-pulse component is undeniably present for specific locations in the ESF, the travel time for most water encountered in the ESF can be safely assumed to be greater than 40 years (i.e., pre-bomb pulse). Under Scenario 2, travel times are assumed to be ≤ 50 ky, such that decay of ^{36}Cl in the samples would be negligible. In this case, variations in the $^{36}\text{Cl}/\text{Cl}$ signals simply reflect variations in the input function and mixing of water parcels with different input ratios. Reconstruction of the input function could be used to estimate apparent travel times, e.g., a sample with a ratio of $1200 (x 10^{-15})$ could only have recharged during limited periods of time when the input value was at least that high (e.g., either 15 ky or 40 ky according to Figure 5). Lower age limits between 0 ky and 15 ky can be established for each of the samples with ratios in the range of $500 (x 10^{-15})$ and $1200 (x 10^{-15})$, by matching their measured ratios with the reconstructed ratios or measured ratios for packrat samples in this period in Figure 5.

Scenario 3: Travel times > 50 ky (mid- to late Pleistocene water). Again, although a bomb-pulse component is undeniably present for specific locations in the ESF, the travel time for most water encountered in the ESF is assumed to range up to several hundred thousand years, such that the input $^{36}\text{Cl}/\text{Cl}$ ratio for some or all of the infiltrating water can be assumed to have been considerably higher than the present-day value. Most of the samples are assumed to reflect some reduction from their initial ^{36}Cl content due to radioactive decay. Upper limits for water travel time are calculated in Table 5 assuming a maximum initial $^{36}\text{Cl}/\text{Cl}$ value of $1500 (x 10^{-15})$. While it is clear that bomb-pulse water has reached the TSw unit via fault and fracture zones, upper limits for water ages in the rock matrix, breccia, and nonactive fractures average about 350 ky and range up to 600 ky (Figures 6 and 7). These latter fractures presumably have a lower extent of connectivity than those with signals indicating the presence of a component of bomb-pulse water.

The above scenarios are meant to represent extreme cases. In reality, the true travel times must be some combination of scenarios 1, 2 and 3, but it will be difficult to distinguish between a decrease in signal strength due to radioactive decay (Scenario 3) from a higher-than-present initial $^{36}\text{Cl}/\text{Cl}$ ratio and decrease due to mixing of old water with younger water (Scenarios 1 and 2). True travel times are probably variably younger than the upper limits calculated for Scenario 3. Resolution of this ambiguity in interpretation can only be resolved through independent lines of evidence, such as alternative isotopic methods for dating water movement and the numerical modeling results presented in Section 6.

5.3 Evidence for Controls of Water Movement

Eleven sites (12 samples) from the TSw had analyzed $^{36}\text{Cl}/\text{Cl}$ values $> 1500 \times 10^{-15}$, indicative of bomb-pulse ^{36}Cl signals. All but one of these sites appear to be in the general vicinity of fault

zones projected from their mapped surface locations, based on a comparison with Figure 1 which shows projected locations of the imbricate fault zone, the Drill Hole Wash fault, and the Sundance fault. However, field and petrographic examination of sampled features within the TSw in the ESF indicates no clear evidence of association with major faults. In fact, most of the TSw samples showing bomb-pulse ^{36}Cl are associated with syngenetic features, mainly cooling joints, lithophysal cavities with intersecting cooling joints, and syngenetic breccias. This result is very significant because it implies that the paths of rapid movement of water from the surface, through the TCw and PTn, and into the TSw, are continuous but may be more complex than individual throughgoing fault traces. It should be noted that at least half of the sites showing a bomb-pulse signal also show some evidence of deformation such as separation of joint walls, minor shearing, and breccia fillings. Whether the deformation was also syngenetic, and therefore not directly associated with the formation of inter-unit flow paths, will require further investigation.

Given a fairly uniform distribution of available flow paths within the TSw, nonuniformities in the distribution of flow paths that have received water with bomb-pulse ^{36}Cl may reflect preferential patterns of water movement or spatial variations in infiltration rates at the surface. The nature of flow paths from the surface, particularly the transmissive features in the PTn, is largely unknown, but these paths must exist. Collection and analysis of samples from the PTn and TCw, plus information from field and modeling studies of water infiltration, will help address this issue. When fracture maps for the TSw section become available from the BuRec, initial observations made in this report will be checked and patterns of fracture attributes that may distinguish fast flow paths will be sought.

5.4 Comparison of ^{36}Cl Results for ESF and Borehole Samples

Measured $^{36}\text{Cl}/\text{Cl}$ ratios for borehole samples presented in previous reports (e.g., Fabryka-Martin et al., 1993, Liu et al., 1995) are systematically lower than the values for ESF samples in this report. This discrepancy is probably attributable to differences in the sample collection techniques. Borehole samples are obtained from ream cuttings. Rock Cl is released to the cuttings during drilling, and subsequently is leached together with the porewater Cl during sample preparation for ^{36}Cl analysis. Correction of the measured $^{36}\text{Cl}/\text{Cl}$ ratio for dilution by rock Cl, which has an extremely low ^{36}Cl content, increases the $^{36}\text{Cl}/\text{Cl}$ value of the meteoric component of Cl in the borehole samples. The ESF samples are not affected by rock Cl to as great an extent because the manual method of collection used in the ESF does not pulverize the rock as does the ream bit.

When the borehole ratios are corrected for the presence of rock Cl, the $^{36}\text{Cl}/\text{Cl}$ ratios are quite similar to the ESF measurements. The method chosen to estimate the proportion of rock Cl present in the borehole samples and hence the magnitude of the $^{36}\text{Cl}/\text{Cl}$ correction factor is the Br/Cl ratio, which is distinctly different between halides derived from the rock and those from the atmosphere. The extent of correction depends on the Br/Cl values selected to represent the rock and meteoric endmembers (Fabryka-Martin et al., 1993).

The Br/Cl ratio for the rock endmember is estimated to be about 0.0017 based on results of experiments in which several Yucca Mountain tuffs were repeatedly ground and leached until a constant Br/Cl value was reached which was assumed to represent the rock endmember (Liu et al., 1995). Determination of the Br/Cl value for the meteoric endmember is not as straightforward. Vegetation tends to concentrate Br whereas plant uptake of Cl is negligible (Brown et al., 1958; Gerritse and George, 1988), so the Br/Cl ratio of the meteoric endmember changes during infiltration through the shallow subsurface, depending upon the residence time of infiltrating water in the root zone. Upper and lower limits for the meteoric Br/Cl ratio are represented by the average value of 0.015 measured for rain water (fracture flow bypassing the root zone) and that of 0.0062 measured for porewater from unconsolidated material below the root zone (matrix infiltration through the root zone) (Fabryka-Martin and Liu, in prep.).

Corrected $^{36}\text{Cl}/\text{Cl}$ results for boreholes UZ-16 and UZ-14 using these bounding values for the meteoric endmember are presented in Tables 6 and 7. Case 1 for these two boreholes corrects the measured $^{36}\text{Cl}/\text{Cl}$ ratios assuming that the average soil porewater Br/Cl ratio best represents the meteoric endmember. This approach results in relatively low $^{36}\text{Cl}/\text{Cl}$ ratios for the TSw samples, ranging from $170 (x 10^{-15})$ to $280 (x 10^{-15})$. Case 2 for these two boreholes corrects the isotopic ratios using the rainwater Br/Cl ratio, giving rise to values ranging from $500 (x 10^{-15})$ to $1500 (x 10^{-15})$, close to the ESF values. The true Br/Cl value of the meteoric endmember is expected to be somewhat in between the two bounding values, a hypothesis supported by the Br/Cl ratio of 0.011 measured for perched water samples (Fabryka-Martin and Liu, in prep.). Refinement of the endmember values for correcting for rock Cl is still under investigation.

6. Flow and Transport Model

6.1 Introduction

The previous section presented conclusions concerning the source of the observed $^{36}\text{Cl}/\text{Cl}$ ratios in the ESF samples. A series of numerical modeling experiments have been run in order to assess the extent to which those conclusions are compatible with current understanding of the hydrogeologic framework of Yucca Mountain and with current estimates of hydrologic parameters. These preliminary studies demonstrate that the observed ^{36}Cl ratios are consistent with existing hypotheses, but do not as yet completely validate them. Using reasonable assumptions for flow and transport processes and parameters, the observed ratios can be explained with the model; but it must be noted that this does not prove that these assumptions are necessarily correct.

The numerical experiments were conducted using FEHM (Finite Element Heat and Mass transfer) (Zyvoloski et al., 1992). FEHM simulates transient, multi-phase, multi-dimensional, non-isothermal, unsaturated, and saturated flow in porous media as well as the simultaneous transport of multiple, chemically reactive and interacting solutes. FEHM has been applied to a comprehensive two- and three-dimensional flow and transport model of Yucca Mountain (Robinson et al., 1996).

The primary goal of the present modeling study is to simulate ^{36}Cl transport to the ESF. The resulting $^{36}\text{Cl}/\text{Cl}$ ratios are a function of the ^{36}Cl input signal (discussed in Section 5.1) and the distribution of travel times for water packets traveling from the ground surface to the sampling point in the ESF. The particle-tracking capabilities of FEHM are used to determine travel-time distributions. This method consists of simulating the simultaneous release of a large number (on the order of 10^9) particles at the ground surface. These particles are carried downward by the vadose-zone flow field. Although the particles all start together, varying flow paths and (optional) hydrodynamic dispersion spread them out into a "cloud" of particles moving through the mountain. Whenever a particle reaches a given observation point (e.g., a sampling point within the ESF), the code records the arrival time. Based on a particle's arrival time at the sampling point (age in the system), the input signal at ground surface when it entered the system is taken from the data set that is plotted in Figure 4. The resulting signal of that particle at the sample location is then computed by correcting for decay. The $^{36}\text{Cl}/\text{Cl}$ signal for a simulated sample of water taken at the location of interest is computed by integrating the signals of all particles arriving at that location. The final output includes a distribution function of particle arrival times and a resulting predicted $^{36}\text{Cl}/\text{Cl}$ ratio for a sample collected at that location.

6.2 Modeling Approach

6.2.1 Simplified, Idealized System

At this preliminary stage, the modeling approach has been greatly simplified. This work will be generalized and expanded for the next report. The model assumes steady-state flow, one-dimensional (1-D) vertical flow, and instantaneous infiltration, and omits hydrodynamic dispersion.

Steady-state flow. To simplify the transport calculations and to minimize the number of variables in this analysis, all simulations assume steady-state flow conditions. These are determined by running an initial flow-only simulation with a specified infiltration rate for a sufficiently long time period ($\sim 10^9$ days) to ensure steady-state conditions. The resulting flow field then defines the initial conditions for ^{36}Cl transport simulations.

1-D columns along ESF. A series of one-dimensional vertical models are constructed at seven stations, spaced at 500-m intervals along the ESF. At each station, the model consists of a vertical column of stacked units, corresponding to the local stratigraphy as described by LANL's three-dimensional stratigraphic model of the mountain (Robinson et al., 1996). The stratigraphy varies along the ESF, as shown schematically in Figure 2. These one-dimensional simulations run very quickly, enabling the analysis of numerous combinations of parameters. The drawback of this approach is that it neglects lateral flow, which previous multi-dimensional studies suggest may be critical (Robinson et al., 1996). However, the large range of infiltration rates analyzed may partially compensate for this drawback, as discussed under "Model Limitations" (section 6.5).

No dispersion. To further simplify these analyses, no dispersion is assumed. Although obviously not realistic, eliminating dispersion removes an entire set of parameters (dispersivities in each rock unit) that would have to be estimated. The result of this assumption is that breakthrough curves and travel-time distributions are unrealistically sharp. This effect will be discussed for specific cases below. A further problem with this assumption is that concentration fronts tend to move as plug flow. For simulating the transport of bomb-pulse ^{36}Cl , which occurred over a period of less than 40 years, this is particularly problematic. The earliest arrival of particles at the ESF may come as a slug with a post bomb-pulse time, for which the associated ^{36}Cl signal has returned to pre bomb-pulse levels, while the next set may come as a slug with a pre-bomb signature. Therefore, in the present analysis, we assumed that the arrival of any particles at the ESF in less than 50 years constitutes bomb-pulse arrival and is recorded as such in Table 9.

Instantaneous Infiltration. In this analysis, we assume that all precipitation that becomes net infiltration (e.g., after evapotranspiration and runoff) moves instantaneously to the first bedrock unit and is not "held up" in the soil zone. For a first analysis, this assumption is reasonable because we suspect that most water that becomes net infiltration arrives in episodic precipitation events and moves quickly into the cap bedrock. In future studies, the impact of retention in the soil zone on $^{36}\text{Cl}/\text{Cl}$ ratios will be examined. This will be done in conjunction with results of studies of spatially variable shallow infiltration, such as that by Flint and Flint (1995), which indicate that shallow infiltration rates are related to alluvial thickness.

6.2.2 Detailed Modeling Approach

Flow and transport are simulated using the dual permeability option in FEHM. With this option, FEHM simulates, in each unit, flow and transport in a fracture continua and a matrix continua, and links the two together through a coupling term which depends on pressure differences between the two continua as well as material properties. This option is described and compared with other conceptual models for simulating flow and transport in fractured porous media in Zyvoloski et al. (1995), Ho et al. (1995), and Robinson et al. (1996).

The modeling effort begins with an in-depth analysis of flow and transport at a single station, Station 35. In the future, results will be extended to other ESF stations. The model domain extends from the ground surface to the water table. The stratigraphy at Station 35 consists of three subunits of the Tiva Canyon welded unit (TCw), three subunits of the Paintbrush Tuff nonwelded unit (PTn), six subunits of the Topopah Spring welded unit (TSw), and four subunits of the Calico Hills nonwelded unit (CHn) (Figure 8). At Station 35, the ESF lies within the TSw3 subunit.

An initial "base case" was defined by setting the flow parameters for all of these subunits to agree with the base case described by Robinson et al. (1996, Table 6-3). The results of the base-case analysis, discussed below, are consistent with the hypothesis that the PTn significantly

retards downward transport. Subsequent simulations address the effects of varying PTn flow parameters.

6.3 Base Case Results

Flow and transport simulations are run for Station 35 using five different infiltration rates: 0.1 mm/yr, 1 mm/yr, 5 mm/yr, 10 mm/yr, and 50 mm/yr. Detailed results of the steady-state flow field for the 1 mm/yr simulation are shown in Figure 8, and transport breakthrough curves at the ESF for the three lower infiltration cases are shown in Figures 9-11.

Figure 8 shows the Station 35 stratigraphic column, steady-state saturation and pressure fields, a plot showing the pressure difference between the matrix and fractures, and estimated $^{36}\text{Cl}/\text{Cl}$ ratios with depth in both the matrix and the fractures, for the 1 mm/yr infiltration case. As expected, matrix saturations are quite high throughout the column, while fracture saturations are low until the capillary fringe near the base of the model is encountered. The pressure fields are far more variable, but are subatmospheric (<0.1 MPa) throughout the column, indicating an absence of any perching fluid. Throughout most of the column, fracture pressure exceeds matrix pressure, indicating flow from the fractures into the matrix; but at two locations in the PTn and the TSw, matrix pressure exceeds fracture pressure, indicating flow from the matrix into the fractures.

The $^{36}\text{Cl}/\text{Cl}$ profiles in Figure 8 show the location of the bomb-pulse in the matrix at the base of the TCw. The pre-bomb-pulse $^{36}\text{Cl}/\text{Cl}$ input signal is clearly preserved in the matrix throughout the TSw and CHn, as can be seen by comparing the ^{36}Cl profile in Figure 8 to the ^{36}Cl input signal in Figures 4 and 5 (e.g., the broad peak in the Figure 8 profile at 1175-1150 m, the valley at 1125 m and the pronounced peak at 1105 m correspond to similar features on figure 5 at 20 to 22 ky, 30 ky, and 40 ky). The $^{36}\text{Cl}/\text{Cl}$ input signal is reproduced in unnaturally sharp detail due to the lack of both dispersion and soil-zone mixing.

The fractures, on the other hand, show a distinctly different pattern. The fractures in the PTn cannot sustain flow at this low (1 mm/yr) infiltration rate, and therefore form a "capillary barrier" to downward transport. Increased saturation at the TCw/PTn interface demonstrates behavior at a capillary barrier. The $^{36}\text{Cl}/\text{Cl}$ profile shows that bomb-pulse ^{36}Cl has also reached this barrier in the fractures, where it is then diverted into the matrix although the flux diverted from the fractures is too small to shift the $^{36}\text{Cl}/\text{Cl}$ ratio in the matrix at this point. Below this diversion point, the fractures are at their no-flow residual saturation, as evidenced by the decreased saturation and the apparent $^{36}\text{Cl}/\text{Cl}$ ratio of zero. (With no flow at all, travel times are infinite, and the $^{36}\text{Cl}/\text{Cl}$ ratio is arbitrarily set to zero).

At the first pressure-difference reversal at the base of the PTn, the fractures are rewetted by water flowing from the matrix, and the fractures assume the same $^{36}\text{Cl}/\text{Cl}$ ratio as in the matrix. With no other sources of water, the fracture $^{36}\text{Cl}/\text{Cl}$ ratio remains constant with depth until an additional influx of water comes in from the matrix at the second pressure reversal, at the

interface between TSw2 and TSw3. At this point, the fracture $^{36}\text{Cl}/\text{Cl}$ ratio once again jumps upward, reflecting the higher Pleistocene signal in the matrix at that point. From there to the water table, flow is consistently out of the fractures, and the $^{36}\text{Cl}/\text{Cl}$ ratio once again stays constant.

The $^{36}\text{Cl}/\text{Cl}$ profiles in Figure 8 indicate that bomb-pulse ^{36}Cl has not yet reached the level of the ESF; and that both fractures and matrix at the ESF contain Pleistocene water (i.e., older than 10 ky) with a $^{36}\text{Cl}/\text{Cl}$ ratio between $500 (x 10^{-15})$ and $1000 (x 10^{-15})$. This is confirmed by Figure 9, which shows fracture and matrix breakthrough curves for the ESF. This figure shows that approximately 76% of the flow past the ESF is in fractures, and 24% in the matrix. Of the fracture component, none is younger than 10 ky, and the vast majority of particle ages are in the range of 20 ky to 40 ky. The matrix water is even older, mostly around 50 ky. These waters do not contain any bomb-pulse ^{36}Cl . A comparison of these water ages with the $^{36}\text{Cl}/\text{Cl}$ input signal in Figure 4 shows that this mixture of matrix and fracture water would be expected to have $^{36}\text{Cl}/\text{Cl}$ ratios in the range of $500 (x 10^{-15})$ to $1000 (x 10^{-15})$.

Figures 10 and 11 show analogous breakthrough curves for lower and higher infiltration rates of 0.1 mm/yr and 5 mm/yr, respectively. At the lower infiltration rate, the entire system is drier and the fractures conduct virtually no flow, while at the higher infiltration rate, fracture flow is increasingly dominant. In both of these cases, the ages of most of the matrix water in the ESF range from 30 ky to 300 ky. Ages of water in the fractures in the ESF are less than those in the matrix. In the high infiltration rate case, for example, most of the fracture water ranges in age from 2.5 ky to 4.5 ky. However, even assuming an extreme infiltration rate as high as 50 mm/yr does not lead to bomb-pulse ^{36}Cl in either matrix or matrix fluids in the ESF tunnel, with these base case parameters.

The present analysis demonstrates that with these base-case parameters, water at the ESF is predicted to be old, with a ^{36}Cl ratio between $500 (x 10^{-15})$ and $1000 (x 10^{-15})$. This is consistent with the ratios measured for systematic samples collected in the ESF, and for those feature-based samples that contain no bomb-pulse component. With these parameters, no reasonable infiltration rate can move bomb-pulse ^{36}Cl into the ESF because fracture flow is not sustained through the entire thickness of the PTn. Some ESF samples, however, clearly do show a bomb-pulse signature, indicating rapid transport. The next section explores what parameter changes would be necessary to enable such transport.

6.4 Effects of PTn Parameters on Rapid Transport

6.4.1 Introduction

The data plotted in Figure 3 show a series of $^{36}\text{Cl}/\text{Cl}$ signals measured from systematic and feature-based samples of TSw tuff, distributed within the range of $500 (x 10^{-15})$ to $1300 (x 10^{-15})$. At five discrete features characterized by fractured zones relating to faulting or other disturbances, $^{36}\text{Cl}/\text{Cl}$ signals range as high as $4000 (x 10^{-15})$. These measurements indicate

isolated pathways of bomb-pulse conductance, and this section provides an introductory examination of parameters and processes that would lead to a bomb-pulse ^{36}Cl signal at the ESF in isolated locations. The working hypothesis is that the bomb-pulse ^{36}Cl signal penetrates into the ESF through discrete flow pathways characterized by different percolation flux and/or material properties than are found in the flow pathways taken by fluid to ESF sample locations at which no bomb-pulse is found. In other words, infiltration changes at the surface and property changes in the PTn, both of which may result from faulting or other disturbances, are examined as potential mechanisms for isolated fast flow paths connecting the TCw to the TSw.

The base-case analysis shows that fracture flow cannot be sustained through the entire thickness of the PTn. Thus, even though most of the flow in the TSw occurs in fractures under high infiltration model simulations, the time-limiting process for rapid travel times from the surface to the ESF is travel time in the PTn. This section examines the hydrologic parameters of the PTn in order to assess what variation from the base-case parameters is required to simulate rapid movement through the entire PTn. This analysis shows that for infiltration rates greater than 1 mm/yr, if fracture flow can be sustained through the entire PTn unit, then it is possible to simulate arrival of bomb-pulse ^{36}Cl into the ESF tunnel. However, even at an infiltration rate of 5 mm/yr, when the PTn fracture parameters are changed to sustain fracture flow, the fraction of infiltrating water reaching the ESF that could contain bomb-pulse ^{36}Cl is substantially less than 1% of all water flowing through that sample location. Whereas the present analysis only addresses what type of parameter changes lead to any bomb-pulse ^{36}Cl arrivals at the ESF, future studies will evaluate how much bomb-pulse ^{36}Cl is necessary to yield $^{36}\text{Cl}/\text{Cl}$ ratios similar to the "clear bomb-pulse" measurements shown in Figure 3.

6.4.2 Definition of Cases

The base-case analysis indicated that the limiting factor in transporting bomb-pulse chloride to the ESF is fracture transport through the PTn. We therefore focussed our sensitivity study on those parameters that control PTn fracture transport. In our implementation of the FEHM code, the fracture network is assumed to act like a continuous porous medium with van Genuchten unsaturated behavior. Fracture transport is controlled by 5 parameters: fracture porosity (ϕ_f), fracture permeability (k_f), matrix block length scale (L_b), and two van Genuchten parameters (α_f and n_f). The porosity controls the total fraction of rock volume that is contained in fractures, the permeability controls the saturated hydraulic conductivity of an individual fracture (effective conductivity of the fracture continuum varies with $\phi_f \cdot k_f$), the matrix block length scale affects the degree of connection between a fracture node and its corresponding matrix node, and the two van Genuchten parameters control the unsaturated behavior of the fracture. Rather than varying these five parameters independently, we recognized that they are interrelated to some extent, and can be considered as functions of two "master parameters," fracture density and effective fracture aperture. (The one exception to this generalization is n_f , a van Genuchten fitting parameter. Following the discussion by Wilson et al., 1994 (their section 14.5.4), we have set $n_f = 3.0$ for all of our simulations.) We postulate that the changes in PTn fracture properties that permit continuous fracture transport are due to some mechanical disturbance of the PTn that increased

fracture density and/or fracture aperture. Our various test cases defined below represent changes in these two master parameters. Changing these master parameters affects the model parameters as follows:

- ▶ Increased fracture aperture: ϕ_f and α_f increase linearly with increased fracture aperture, k_f increases with the square of fracture aperture, and L_f is not a function of aperture.
- ▶ Increased fracture density: ϕ_f increases linearly with increased fracture density, L_f decreases with the inverse of fracture density, and α_f and k_f are not a function of fracture density.

Within this framework, we have defined three simulation cases that represent perturbations in the PTn of the base case defined earlier.

Case A. Doubles the fracture density of the base case.

Case B. Doubles the effective fracture aperture of the base case.

Case C. Doubles the fracture density and the fracture aperture of the base case.

Previous work (Robinson et al., 1996, sec 6.5.3) has pointed out the uncertainty associated with α_f and the model's sensitivity to that parameter. We therefore added two additional simulation cases to further explore α_f .

Case D. Identical to base case, with α_f decreased by one order of magnitude (from 10 m^{-1} to 1.0 m^{-1}).

Case E. Identical to Case C, with α_f decreased by a factor of 20 (from 20 m^{-1} to 1.0 m^{-1}).

PTn fracture parameters for the base case and Cases A-E are shown in Table 8.

6.4.3 Modeling Results for PTn Parameter Variation Study

A series of simulations were run for Station 35 in which parameters in the PTn were changed as described above. Infiltration rates of 0.1, 1, 5, 10, and 50 mm/yr were considered. Table 9 gives arrival times of the first 1%, 5%, and 50 % of the water arriving in the matrix and in the fractures at the ESF for these simulations. It also indicates whether any bomb-pulse ^{36}Cl (always less than 1% of the fracture flow, if present at all) arrives. For each infiltration rate, the percent of all water arriving at the ESF in the fracture and matrix is indicated. It is not surprising that for these steady state simulations, these percentages of matrix and fracture flow at the ESF do not change for cases of different PTn properties at the same infiltration rate because the ESF is not located in the PTn at Station 35.

For the base-case properties, no bomb-pulse ^{36}Cl arrives at the ESF in the simulations for any of these infiltration rates. Arrival times steadily decrease with increasing infiltration rate because the relative permeability of the matrix material in the PTn increases with saturation, which in

turn increases with infiltration rate. However, the fractures do not sustain flow through the entire thickness of the PTn for any of these base-case conditions. Within the range of 1 mm/yr to 10 mm/yr, the resulting $^{36}\text{Cl}/\text{Cl}$ signal at the ESF is consistent with that measured for the systematic samples in the ESF. Hydrodynamic dispersion and soil-zone mixing are not considered at this time but, for those infiltration rates, median ages at the ESF between 28 ky and 54 ky, with no bomb-pulse ^{36}Cl , would correspond to $^{36}\text{Cl}/\text{Cl}$ ratios between 500 ($\times 10^{-15}$) and 1200 ($\times 10^{-15}$). The analysis summarized in this section begins with an infiltration rate of 5 mm/yr and examines what property changes in the PTn lead to sustained fracture flow, and hence rapid travel times to the ESF. When parameter changes result in bomb-pulse arrival at the ESF for 5 mm/yr infiltration rate, the infiltration rate is dropped to 1 mm/yr in order to assess the effect at a lower infiltration rate. When no bomb-pulse is found in the ESF, the infiltration rate is increased to 10 mm/yr.

For an infiltration rate of 5 mm/yr, results for the base case and cases A to E are plotted in Figures 11-16, respectively, and are summarized below. The results of all simulations are summarized in Table 9. The plots use a log-log scaling in order to highlight the cases in which bomb-pulse ^{36}Cl arrives at the ESF as well as to show the relatively small amount of bomb-pulse associated with those cases. As mentioned above, the partitioning of flow between fractures and matrix at the ESF remains virtually identical in each of these cases, regardless of whether bomb-pulse ^{36}Cl arrives at the ESF. The only difference is whether the PTn can sustain fracture flow and hence provide a bomb-pulse ^{36}Cl at the top of the TSw:

- Base Case** As described above, the base-case properties were taken from Table 6-3 in Robinson et al. (1996). For these properties and an infiltration rate of 5 mm/yr, the matrix water age is mostly around 30 ky while the fracture water age range is mostly between 2.5 ky and 4.5 ky. No bomb-pulse ^{36}Cl arrives at the ESF.
- Case A** Doubling fracture density does not significantly change the travel time of ^{36}Cl from the surface to the ESF. Although the overall fracture network permeability in the PTn increases, the reduced length scale of connectivity allows for greater flow from the fractures into the matrix. By the bottom of the PTn, all flow in the fractures has entered the matrix. Hence, the overall travel time to the ESF is limited by the PTn matrix travel time. Increasing the infiltration rate to 10 mm/yr does not yield bomb-pulse ^{36}Cl in the ESF either.
- Case B** Doubling effective fracture aperture allows some fracture flow to be sustained throughout the entire PTn. At an infiltration rate of 5 mm/yr, most flow in the TSw is in the fractures. Hence, fluid arriving at the bottom of the PTn in fractures enters the TSw and continues to flow predominantly in the fractures of that unit. This results in the arrival of a very small amount of fluid at the ESF that is less than 50 years old, i.e., bomb-pulse ^{36}Cl . However, the quantity of bomb-pulse water arriving at the ESF for this set of parameters is less than 0.1% of the total flux of water arriving at the ESF. The rest of the water is a mixture of water that has traveled along a path of matrix and fracture flow in the PTn and then as fracture and

matrix flow in the TSw. As with the base case and Case A, the matrix water age is mostly about 30 ky and the fracture water age is mostly between 2.5 ky and 4.5 ky. When the infiltration rate is decreased to 1 mm/yr, fracture flow is no longer sustained in the PTn and no bomb pulse arrives at the ESF.

- Case C** Although doubling both fracture density and fracture aperture results in the highest overall fracture network permeability, the reduced fracture spacing (and increased matrix influence) controls the flow system such that fracture flow through the entire PTn cannot be sustained. The resulting breakthrough at the ESF is controlled by matrix flow rates in the PTn, and the curve is similar to that plotted for the base case (Figure 8) and for Case A (Figure 9). However, increasing the infiltration rate to 10 mm/yr does yield bomb-pulse ^{36}Cl in the ESF.
- Case D** Starting with base-case parameters, but reducing the fracture α in the PTn units to 1 from 10 permits some fracture flow through the PTn. In this case, bomb-pulse ^{36}Cl reaches the ESF. Again, the portion of flow attributed with bomb-pulse signal is substantially less than 1%. When the infiltration rate is decreased to 1 mm/yr, fracture flow is no longer sustained in the PTn and no bomb pulse arrives at the ESF.
- Case E** Increased fracture aperture and density in the PTn (Case C) did not lead to simulated bomb-pulse arrivals at the ESF. However, by decreasing fracture α in the PTn to 1 (the difference between Cases C and E), fracture flow was sustained in the PTn and bomb pulse arrivals at the ESF were simulated. Bomb pulse arrival of ^{36}Cl is also observed for this case when the infiltration rate is reduced to 1 mm/yr.

6.5 Modeling Limitations

6.5.1 FEHM Conceptualization

These simulations were performed using FEHM, and are subject to the assumptions and conceptualization inherent in that code. Chief among these are the dual-permeability formulation, which models the fracture network and the matrix as two superimposed continuous porous media. In our implementation, we have further specified that these continua follow van Genuchten unsaturated flow behavior, and that the system is isothermal. These assumptions are common to much of the flow and transport modeling associated with YMP, and it is beyond the scope of this report to discuss them further. Discussion of the model formulation can be found in Ho et al. (1995) and Robinson et al. (1996).

6.5.2 1-D analysis -- no lateral flow or anisotropy

Performing these simulations in one dimension greatly simplified the conceptualization and reduced computing time, thereby enabling the large number of simulations discussed above.

Although one-dimensional analysis may be valid on a system limited to or dominated by one-dimensional processes, previous simulations at Yucca Mountain have demonstrated the potential importance of lateral flow diversion at geologic contacts (Robinson et al., 1996).

What are the implications of using one-dimensional analyses to model what is probably an inherently multi-dimensional system? The most obvious effect of the one-dimensional analysis is the complete elimination of any opportunity for lateral flow. In this simulation, all water that infiltrates at the ground surface must move vertically down through the stratigraphic section; there is nowhere else it can go. In reality, the capillary barrier at the TCw/PTn contact and the permeability contrast at the PTn/TSw contact may laterally divert flow down dip. In the 1-D simulation, there is no "down dip," and saturations build up at the contacts, leading to increased vertical matrix flow. Therefore, these simulations cannot directly address the effectiveness of geologic contacts as barriers to downward flow.

This is not as severe a limitation as it may at first appear. Although some attention has been paid to the concept of an "impermeable barrier" at the PTn/TSw contact, this is clearly not the case. The ^{36}Cl data presented in this report clearly demonstrate that there is at least some downward flow through the PTn throughout the sampled portion of the ESF tunnel because, in the absence of any flow, observed ^{36}Cl ratios would be roughly 20 ($\times 10^{-15}$), in equilibrium with the *in-situ* neutron flux (Fabryka-Martin et al., 1993). As discussed above, the actual values, ranging from 500 ($\times 10^{-15}$) to 1200 ($\times 10^{-15}$), suggest that water is indeed moving down to the ESF level. The $^{36}\text{Cl}/\text{Cl}$ ratios demonstrate that the capillary barrier is not impermeable, that lateral flow does not divert 100% of the water in the TCw. Flow that is not diverted moves vertically down into the PTn, and its behavior can then be approximated using 1-D models. The decrease in flow caused by lateral diversion is accounted for by decreasing the infiltration rate.

This adjustment for lateral diversion then raises the question of the fate of the diverted water. As Robinson et al. (1996, sec. 6.5.2) point out, the diverted water must move down towards the water table eventually. In their model, they found downward movement at two locations: along the Ghost Dance Fault, and along the boundary of the model. The latter is a modeling artifact, but downward movement along a fault zone is a realistic explanation. The model that produced this result does not explicitly include a fault with distinct parameters; rather, the disruption of lateral flow is caused by a vertical offset in the geology. At the scale of the model, these offsets are limited to mapped fault zones and are few and far-between, while in reality, field mapping (in the ESF and elsewhere) has revealed numerous instances of small offsets. Many of these offsets have the potential of disrupting lateral flow and producing vertical flow. Vertical flow moving downward from these sources can be approximated using a 1-D model, with an increased infiltration rate.

It is clear that a one-dimensional model cannot directly account for lateral flow diversion. In this case, however, it seems likely that lateral flow processes will divert vertical flow away from some areas, and concentrate it in others. These two different areas can be independently modeled in 1-D, using a range of different infiltration rates. For example, let us assume that the overall

average infiltration rate is 1 mm/yr. Lateral diversion may decrease the effective vertical flow over much of the region to 0.5 mm/yr, and increase flow at a few locations to 10 mm/yr. In this hypothetical example, the resulting range in travel time behavior could be approximated using a 1-D model with a range in infiltration rates of 0.5 to 10 mm/yr. However, if the lateral diversion occurs at the PTn/TSw interface, then the present model does not accurately capture that effect and overestimates the potential for fracture flow in the PTn.

This argument suggests that the 1-D results reported in this document may not be unreasonable, and represent a worthwhile scoping effort. Future analyses will include fully two- and three-dimensional simulations, and these issues will then be revisited.

6.5.3 Steady-State Flow

Episodic infiltration may lead to short pulses of very high infiltration, followed by extended dry periods. Whether this affects travel times to the ESF depends on whether or not the PTn "smooths" these pulses. If PTn fractures cannot sustain flow and all flow through the PTn is forced through the matrix, this smoothing probably occurs and the steady-state assumption is valid. On the other hand, it is possible that for cases with continuous fracture flow through the PTn all the way to the ESF, that infiltration pulses may affect travel times to the ESF. This needs to be further investigated.

6.5.4 No Dispersion or Soil-zone Mixing

As stated, these simulations include neither hydrodynamic dispersion nor soil-zone mixing. This simplification caused the unnaturally sharp breakthrough curves presented in the results (sections 6.3 and 6.4.3). Adding dispersion and mixing to the model will tend to broaden the curves. (For example, the broadening of the bomb-pulse ^{36}Cl signal is shown as a function of residence time in the soil in Appendix B of Fabryka-Martin and Liu, in prep.). In those cases that predict very long travel times, on the order of 10^5 years, this will probably have very little substantive effect on the conclusions. For those cases with shorter travel times, dispersion-induced spreading can significantly accelerate early breakthrough, and may lead to predicted bomb-pulse signatures at the ESF in a few cases, such as the base case with an infiltration rate of 50 mm/yr. We do not expect that incorporation of these processes would change the overall conclusions of our study, but we intend to explore the effects of dispersion in future work.

6.6 Discussion of Modeling Effort

Using models to simulate chloride transport requires specifying the infiltration rate and property of the media through which flow and transport occur. Although work is ongoing in the Project to characterize both, neither is without uncertainty. Therefore, within the scope of this work, the current approach is to use a reasonable set of properties which yield simulated results consistent with the systematic samples collected in the ESF. Then, to explain (or predict) the distinct feature-based samples in which bomb-pulse ^{36}Cl is found, the infiltration rate and/or PTn

material values are modified to represent effects in a zone disturbed by processes such as faulting. Presently, the material modifications are made only in the PTn because the ability of that unit to sustain fracture flow determines whether bomb-pulse ^{36}Cl arrives at the ESF in these simulations.

This analysis demonstrates that starting with a reasonable set of base-case properties, ^{36}Cl signals can be simulated at the ESF which are consistent with the systematic samples collected there. By modifying the properties of the fractures to represent greater fracture density and/or increased fracture aperture in fault or fracture zones, arrivals of bomb-pulse ^{36}Cl can be simulated at the ESF. Further, by increasing infiltration rate in conjunction with property modifications, bomb-pulse arrivals at the ESF are predicted in all cases except Case A for base-case infiltration of 1 or 5 mm/yr and Case C for base-case infiltration of 1 mm/yr. Increasing the infiltration rate captures either increased local infiltration above fault zones due to the disturbance at the surface and in the caprock (e.g. reduced evapotranspiration due to rapid vertical downward flow of precipitation). It also captures the effect of increased percolation due to lateral diversion turning into vertical flow in a fault zone.

7. Conclusions

In order to assess groundwater travel times and to identify potential fast paths for infiltrating water, the distribution of ^{36}Cl in the ESF tunnel has been determined by analyses of rock samples from 52 locations between Stations 2 and 36. Rock samples were collected systematically every 200 m throughout the tunnel as well as from diverse geologic features such as faults, fractures, and lithophysal cavities. All of the systematic samples as well as most of the feature-based samples contain ^{36}Cl levels consistent with travel times exceeding a few thousand years. Upper age limits range up to several hundred thousand years. Uncertainties about temporal variations in the atmospheric $^{36}\text{Cl}/\text{Cl}$ input ratio prevent calculation of more precise ground-water travel times at this time. Bomb-pulse levels of this isotope occur at a few distinct fractured and/or faulted zones, indicating that at least a small proportion of the water at these locations is less than 50 years old.

A flow and transport model using the FEHM code is used to simulate transport of ^{36}Cl into the ESF tunnel. Modeling results show that observed ^{36}Cl signals are consistent with existing site conceptual models and parameter estimates. Base-case parameters predict Pleistocene-aged water in the ESF, while parameter changes consistent with faults and fracturing lead to a prediction of a small component of bomb-pulse ^{36}Cl in ESF fractures. Thus, these modeling results show that the new ^{36}Cl data presented in this report do not require a major re-evaluation of previous work.

8. Suggestions for Future Work

- ▶ Continue collecting and analyzing samples from the ESF as the TBM progresses in order to identify potential fast paths and to establish limits on groundwater travel times.

- ▶ Collect and analyze samples from the section in which the PTn is exposed, in order to assess the extent to which vertical movement of ground water is delayed or diverted by this stratigraphic unit.
- ▶ Analyze mineral separates for ^{36}Cl , which would remove uncertainties related to correction procedures for Cl derived from the rock matrix or from construction water and which should be more directly comparable to the U-Th study results (Paces, 1996).
- ▶ Obtain independent verification of the ESF ^{36}Cl results by analyzing cuttings samples from boreholes near the ESF tunnel (SD-7, SD-9, SD-12, NRG-4, NRG-5, NRG-6, NRG-7/7A; see Figure 1).
- ▶ Establish bounding limits on temporal variations of the meteoric $^{36}\text{Cl}/\text{Cl}$ ratio, through additional analysis of packrat samples, literature reviews, and production rate modeling.
- ▶ Evaluate the extent to which ^{36}Cl analyses of secondary minerals may be used in conjunction with mineral deposition ages based on U-Th disequilibria measurements, to assess temporal variations in the meteoric $^{36}\text{Cl}/\text{Cl}$ signal.
- ▶ Extend the transport modeling study using FEHM to other ESF stations so as to present a quasi three-dimensional distribution of travel times for fracture and matrix fluids.
- ▶ Study the effects of the simplifying assumptions used in this study.
- ▶ Investigate the effects of lateral flow in the PTn with two- and three-dimensional models.
- ▶ Examine the effects of transient, episodic infiltration events on flow and transport from the surface to the ESF.
- ▶ Derive age limits based upon improved understanding of ^{36}Cl signal variations, using insights gained from transport modeling.

Acknowledgments

This work was supported and managed by the U.S. Department of Energy, Yucca Mountain Site Characterization Office. New YMP data contained in this report are found in YMP laboratory notebooks TWS-INC-7-04-92-04, LA-CST-NBK-95-032, LA-EES-1-NBK-96-001, and LA-EES-1-NBK-96-002. The data presented were developed under YMP quality assurance (QA) procedures and have been technically reviewed. The formal technical review required by the LANL/YMP QA program will be completed prior to publication of the data in a Level 3 milestone report due in August 1996. The record package containing traceability information is LA-CST-TIP-96-001. The YMP Test Coordination Office supported field sample collection in the ESF tunnel. Ion chromatographic analyses were conducted by Laura Wolfsberg. Mitch Plummer selected and prepared the packrat samples for analysis, and compiled information relevant to interpretation of the results. Extensive laboratory assistance, data review and editorial reviews of early drafts were provided by Dana Brenner. Jeff Roach assisted in sample collection and processing. Pankaj Sharma and other staff at the PRIME Laboratory are thanked for providing prompt turnaround of ^{36}Cl analyses in order to meet this report deadline. Stephen Henderson provided great assistance with particle tracking code development and simulations. Gilles Bussod reviewed this report and provided valuable suggestions.

References

- Brown, A.L., J.J. Jurinak, and P.E. Martin (1958). Relation of soil properties to Br uptake by plants following soil fumigation with ethylene dibromide. Soil Science, 86:136-139.
- Fabryka-Martin, J.T., S.J. Wightman, W.J. Murphy, M.P. Wickham, M.W. Caffee, G.J. Nimz, J.R. Southon, P. Sharma (1993). Distribution of chlorine-36 in the unsaturated zone at Yucca Mountain: an indicator of fast transport paths. Proc., FOCUS '93: Site Characterization and Model Validation, held 26-29 September 1993, Las Vegas, NV (American Nuclear Society: La Grange Park, Illinois), pp. 58-68.
- Fabryka-Martin J.T., and B. Liu (in prep.). Distribution of chlorine-36 in UZ-14, UZ#16, perched water, and the ESF North Ramp, Yucca Mountain, Nevada. Los Alamos National Laboratory, YMP Milestone Report M3431 (draft approved by YMSCO, being revised for publication).
- Flint, A.L., and L.E. Flint (1995). Spatial distribution of potential near surface moisture flux at Yucca Mountain, Proceedings of the 5th Annual Intl. Conf. on High Level Radioactive Waste Management, Las Vegas, NV, May 22-26, 1994, p. 2352-2358.
- Gerritse, R.G., and R.J. George (1988). The role of soil organic matter in the geochemical cycling of chloride and bromide. J. Hydrology, 101:83-95.
- Ho, C.K., S.J. Altman, and B.W. Arnold (1995). Alternative conceptual models and codes for unsaturated flow in fractured tuff: preliminary assessments for GWTT-95, Sandia National Laboratory Technical Report SAND95-1546.
- Liu, B., J. Fabryka-Martin, A. Wolfsberg, B. Robinson, and P. Sharma, (1995). Significance of Apparent Discrepancies in Water Ages Derived from Atmospheric Radionuclides at Yucca Mountain, Nevada, in Water Resources at Risk, W. R. Hotchkiss, J. S. Downey, E. D. Gutentag and J. E. Moore, eds. (American Institute of Hydrology, Minneapolis, Minnesota), pp. NH-52 - NH-62.
- Mazaud, A., C. Laj, E. Bard., M. Arnold, and E. Tric (1991). Geomagnetic control of ^{14}C production over the last 80 ky: Implications for the radiocarbon time-scale. Geophysical Research Letters, 18: 1885-1888.
- Paces, J.B. (1996). Memorandum to R.W. Craig dated February 23, 1996, concerning "Submission of milestone 3GQH455, due February 29, 1996."
- Phillips F.M., P. Sharma, and P. Wigand (1991). Deciphering variations in cosmic radiation using cosmogenic ^{36}Cl in ancient rat urine, Amer. Geophy. Union Fall Meeting Program and Abstracts, 72.

- Plummer, M. (1996). Secular variation of cosmogenic isotope production as measured in fossil packrat middens. Unpublished M.Sc. thesis, New Mexico Tech, Socorro.
- Robinson, B.A., A.V. Wolfsberg, C.W. Gable, and G.A. Zyvoloski (1996). An unsaturated zone flow and transport model of Yucca Mountain, Los Alamos National Laboratory, YMP milestone 3468, submitted to YMPO October, 1995, in comment resolution.
- Tric, E., J.-P. Valet, P. Tucholka, M. Paterne, L. LaBeyrie, F. Guichard, L. Tauxe, and M. Fontugne (1992). Paleointensity of the geomagnetic field during the last 80,000 years, J. Geophysical Research, 97: 9337-9351.
- Tyler, S.W., J.B. Chapman, S.H. Conrad, D.P. Hammermeister, D. Blout, J. Miller, and J.M. Ginanni (in press). Soil water flux on the Nevada Test Site: spatial and temporal variations over the last 120,000 years. Water Resources Research.
- Valet, J.-P., and L. Meynadier (1993). Geomagnetic field intensity and reversals during the past four million years. Nature: 366, 234-238.
- Wilson, Michael L., et al. (1994). Total-System Performance Assessment for Yucca Mountain - SNL Second Iteration (TSAP-1993). Sandia National Laboratories Report SAND93-2675.
- Zyvoloski, G.A., Z.V. Dash, S. Kelkar (1992). "FEHMN 1.0: Finite Element Heat and Mass Transfer Code", Los Alamos National Laboratory Report, LA-12062-MS, Rev.1.
- Zyvoloski, G.A., B.A. Robinson, Z.V. Dash, and L.L. Trease (1995). Models and methods summary for the FEHMN application, Los Alamos National Laboratory Report, LA-UR-94-3787, Rev 1.

Table 1. ESF samples collected for ³⁶Cl analysis, November 1995 to February 1996 (see note)

Approx. ESF station	SMF barcode	LANL ID	Sampled feature	Field description
1+98	507923	E001	Fault zone	Bow Ridge Fault, Tiva Canyon tuff wallrock (collected by US BuRec, Feb 1995)
1+99	509016	E008	Fault zone	Bow Ridge Fault, gouge (collected by US BuRec, Apr 1995)
1+99	509017	E009	Fault zone	Bow Ridge Fault, gouge (collected by US BuRec, Apr 1995)
1+99	509018	E010	Fault zone	Bow Ridge Fault, gouge (collected by US BuRec, Apr 1995)
1+99	509019	E011	Fault zone	Bow Ridge Fault, rubble (collected by US BuRec, Apr 1995)
1+99	509020	E012	Fault zone	Bow Ridge Fault, gouge (collected by US BuRec, Apr 1995)
2+3	507924	E007	Fault zone	Bow Ridge Fault, pre-Rainier Mesa tuff wallrock, zeolitic (collected by US BuRec, Feb 1995)
4+94	512551	E163	Systematic	Systematic sampling of PTn bedrock
5+4	504280	E073	Fault?	Breccia (collected by US BuRec, 1995)
5+5	503866	E074	Fault?	Breccia (collected by US BuRec, 1995)
7+0	512550	E164	Systematic	Systematic sampling of PTn bedrock
7+70	512549	E165	PTn contact	Tpcpln/Tpcpv contact, ~ 1 m above contact
7+70	512548	E166	PTn contact	Tpcpln/Tpcpv contact
7+70	512547	E167	PTn contact	Tpcpln/Tpcpv contact, ~ 1 m below contact
8+59	512546	E168	PTn contact	Tpcpv/Tpbt4 contact, ~ 1 m above contact
8+59	512545	E169	PTn contact	Tpcpv/Tpbt4 contact
8+59	512544	E170	PTn contact	Tpcpv/Tpbt4 contact, ~ 1 m below contact
8+90	512554	E171	PTn contact	Tpbt3/Tpp contact, ~ 1 m above contact

Approx. ESF station	SMF barcode	LANL ID	Sampled feature	Field description
8+90	512553	E172	PTn contact	Tpbt3/Tpp contact
8+90	512552	E173	PTn contact	Tpbt3/Tpp contact, ~ 1 m below contact
9+0	512543	E174	Systematic	Systematic sampling of PTn bedrock
11+0	503935	E027	Systematic	Systematic sampling of TSw bedrock
11+43	510583	E086	Bedrock	Unaltered TSw (collected by US BuRec, 1995)
12+44	503934	E028	Cooling joints	Vertical cooling joints and intervening horizontal cooling joints
13+0	503932	E029	Systematic	Systematic sampling of TSw bedrock
13+67	503931	E030	Cooling joints	Weakly cemented rubble from shear zone at intersection with another shear zone
14+0	503930	E031	Shear zone	Broken rock from shear zone
14+14	503929	E032	Shear zone	Broken rock from shear zone
14+41	503928	E033	Fault	Calcite-cemented breccia from fault at intersection with fracture
15+0	503926	E034	Systematic	Systematic sampling of TSw bedrock
15+5	503925	E035	Fracture	Calcite-lining fracture; calcite-cemented breccia
16+0	509248	E016	Fracture	
16+12	509242	E036	Cooling joint	Separated cooling joint with calcite infilling
16+19	509241	E037	Fracture	Clay-rich fracture fill
17+0	503924	E038	Systematic	Systematic sampling of TSw bedrock
17+11	503923	E039	Fracture	Calcite and broken rock from fracture
18+96	503922	E040	Broken rock	Bedrock cut by many short-segment, high-angle cooling cracks
19+0	503921	E041	Systematic	Systematic sampling of TSw bedrock
19+31	503920	E042	Breccia zone	Bulk broken rock and breccia

Approx. ESF station	SMF barcode	LANL ID	Sampled feature	Field description
19+37	503919	E043	Fault zone	Bulk broken rock and breccia
19+42	503918	E044	Breccia zone	3-m wide syngenetic rubbly zone, bounded by vertical fractures, with widespread calcite cement
21+0	503917	E045	Systematic	Systematic sampling of TSw bedrock
21+65	509228	E017	Lith cavity	Cavity in otherwise unfractured rock
22+71	503916	E046	Fracture zone	Near-vertical fracture zone about 6-m wide; 40% of rock is lithophysal cavities
22+72	509226	E018	Fault breccia	
23+0	509247	E047	Systematic	Systematic sampling of TSw bedrock
23+86	509246	E048	Fracture	Broken rock
24+37	509245	E049	Cooling joint	Broken rock between 2 cooling joints
24+38	509222	E019	Lith cavity	Cavity intercepted by cooling joint
24+40	509240	E050	Fault zone	Uncemented fault gouge from a near-vertical fault following an old cooling crack
24+68	509220	E020	Fracture	Partly syngenetic rubbly breccia in TSw, frax surfaces coated with vapor-phase silica
25+0	509259	E051	Systematic	Systematic sampling of TSw bedrock
26+79	509244	E052	Shear zone?	Broken rock from 1-meter wide cooling joint zone
26+88	509251	E021	Lith cavity	Silica lining and halo surrounding cavity
26+88	509239	E053	Cooling Joint	Calcite-filled cooling joint in lithophysal zone
26+95	509253	E022	Fracture	Calcite-filled fracture, possibly cooling joint
27+0	509257	E054	Systematic	Systematic sampling of TSw bedrock
27+18	509218	E023	Lith cavity	Cavity adjacent to fault
27+18	509243	E056	Fault	Broken rock from fault separating TSw1 and TSw2

Approx. ESF station	SMF barcode	LANL ID	Sampled feature	Field description
27+50	509238	E057	Fracture	Breccia from fracture, with weak calcite veinlets throughout
27+66	509237	E058	Fault	Fault gouge consisting of clay and breccia with trace of calcite
28+40	509236	E059	Fault	Fault zone with carbonate-cemented breccia
28+80	509215	E024	Lith cavity	Calcite from cavity
28+80	509215	E025	Bedrock	Rock adjacent to above cavity
28+81	503981	E162	Fracture	
29+0	503947	E141	Systematic	Systematic sampling of TSw bedrock
29+21	503983	E142	Fracture	
29+65	503948	E143	Fault	Breccia
29+73	503949	E144	Cooling joint	
29+80	503985	E145	Lith cavity	
30+18	503987	E146	Lith cavity	
30+27	503976	E147	Cooling joints	
31+61	503975	E148	Lith cavity	
31+64	503973	E149	Cooling joint	
33+0	503939	E150	Systematic	Systematic sampling of TSw bedrock
33+16	503990	E151	Lith cavity	Cavity with calcite/opal, intersected by vertical cooling joint
34+28	503993	E152	Fractures	Cooling joints and rubbly rock
34+32	503938	E153	Cooling joints	Broken rock at the intersection of offset cooling joints
34+71	503937	E154	Cooling joints	Breccia in offset cooling joint
35+0	503980	E155	Systematic	Systematic sampling of TSw bedrock
35+0	503969	E156	Cooling joints	Broken rock with throughgoing cooling joints

Approx. ESF station	SMF barcode	LANL ID	Sampled feature	Field description
35+3	503994	E157	Cooling joints	Calcite breccia cement in separated cooling joints
35+8	503995	E158	Cooling joints	Breccia bounded by high-angle cooling joints
35+24	503997	E159	Cooling joint	Calcite from near-vertical cooling joint and adjacent breccia
35+45	503979	E160	Fracture	Broken rock from vertical fractures in a zone of cooling joints
35+58	503999	E161	Cooling joints	Breccia zone bounded by high-angle cooling joint
35+93	512511	E175	Fault	Breccia (possibly Sundance Fault)
36+55	512506	E176	Fault	Fault gouge
37+0	512510	E177	Systematic	Systematic sampling of TSw bedrock
37+60	512504	E178	Fracture	Fracture gouge
37+68	512509	E179	Fracture	Bulk rock and fracture gouge
38+47	512513	E180	Fracture	Fracture and fracture fill minerals
38+62	512515	E181	Lith cavity	Bulk rock and lithophysal cavity
38+79	512502	E182	Fracture	Fracture material/gouge
38+95	512517	E183	Cooling joint	Fracture fill/gouge
39+0	512508	E184	Systematic	Systematic sampling of TSw bedrock (fractured rock)
39+39	503944	E185	Fracture	Lithophysal cavity with calcite
39+47	503943	E186	Cooling joint	Gouge within offset cooling joint
39+61	503946	E187	Cooling joint	Gouge within offset cooling joint

Note: Samples collected earlier in 1995 by the U.S. Bureau of Reclamation as part of the ESF Consolidated Sampling Program are included in the above list if they have been analyzed for ³⁶Cl.

Table 2. PTn samples marked for collection as of 9 February 1996

A.	Systematic sampling every 200 m, Stations 5, 7, 9 (3 samples collected on 9 Feb 96)
B.	Alcove 3, 3 samples from Station 0+18. One sample each from the same two horizontal locations as the USGS temperature/moisture probes, and one sample approximately midway between these two locations. Sampled units: Tpcpln, transition, Tpcpv
C.	Alcove 4, 3 samples from Station 0+51: <ul style="list-style-type: none">▶ one sample from the red argillic horizon▶ one sample above the red argillic horizon, but within 5 to 15 cm of it▶ one sample below the red argillic horizon, but within 5 to 15 cm of it
D.	North Ramp main tunnel, 3 samples from each of the following stratigraphic unit contacts, generally one sample from contact itself (i.e., centered on the contact, and including material within approximately 5 cm of it), a second sample approximately 1 ± 0.25 m above the specified contact, and a third sample 1 ± 0.25 m below the contact. Sta 7+70: Tpcpln/Tpcpv2 contact (3 samples collected on 9 Feb 96) Sta 8+29: Tpcpv1/Tpbt4 contact Sta 8+59: Tpcpv/Tpbt4 contact (3 samples collected on 9 Feb 96) Sta 8+73: Tpbt3, contact between coarse and fine subunits Sta 8+90: Tpbt3/Tpp contact (3 samples collected on 9 Feb 96) Sta 10+55: Tpcrv2/Tpcrv1 contact Sta 10+60: 2 m above Tpcrv2/Tpcrv1 contact (1 sample only)
E.	1 consolidated sample from the North Ramp main tunnel, from the highly fractured zone at Station 10+88
	Number of stations marked: 13
	Number of samples marked: 29
	Number of samples collected: 12

Note: stratigraphic unit designations are only preliminary at this stage.

Table 3. Summary of samples collected, by feature

Sampled feature	No. of locations (Note)	No. of samples
Systematic samples		
▶ Systematic sampling in TSw	14	14
▶ Systematic sampling in PTn	3	3
▶ Other intact bedrock	1	1
Feature-based samples		
▶ Fractures, faults, lithophysal cavities	65	72
▶ Unit contacts in the PTn	3	9
TOTAL	86	99

Note: Structural features, especially fault zones and zones of broken rock, often span one or more meters of the tunnel wall. In these cases, samples were considered to be from the same location if they were collected within 10 meters of one another.

Table 4. Analyses of J#13 well water and ESF construction water

LANL ID	Collection date	Source	Cl, mg/L	Br, mg/L	Br/Cl ratio	³⁶ Cl/Cl x 10 ⁻¹⁵
J#13 well water (source used to prepare ESF construction water)						
W101	22-Mar-95	J#13 wellwater	7.02	0.051	0.0073	505 ± 9
ESF construction water samples, from makeup tank to point of use						
W112	31-Jan-96	Makeup tank	6.72	19.9	3.0	---
W123	09-Feb-96	Makeup tank	6.67	21.5	3.2	---
W119	31-Jan-96	Outlet at Alcove #2 portal	6.68	19.9	3.0	---
W121	31-Jan-96	Outlet in Alcove #3	6.67	19.7	3.0	---
W122	09-Feb-96	Outlet in Alcove #4	6.64	21.1	3.2	---
W120	31-Jan-96	Outlet near TTF alcove	6.79	20.6	3.0	---
W114	31-Jan-96	Outlet, CS 35+89	6.67	19.9	3.0	---
W096	27-Apr-95	TBM water jet	8.90	19.5	2.1	492 ± 10
W116	31-Jan-96	TBM supplemental drill deck	6.67	19.9	3.0	---
W117	31-Jan-96	TBM Deck-14	6.71	20.0	3.0	---
W118	31-Jan-96	TBM primary drill deck	6.71	20.1	3.0	---
ESF construction water samples after use						
W115	31-Jan-96	Belt water near Alcove #1	25.8	43.8	1.7	---
W113	31-Jan-96	Recovery tank	13.1	27.5	2.1	---
W124	09-Feb-96	Recovery tank	11.5	28.3	2.5	---
W110	27-Dec-95	Dripping rock bolt, Alcove #3	7.87	22.3	2.8	---
W111	27-Dec-95	Dripping rock bolt, Alcove #3	9.59	28.3	3.0	---

Note: ³⁶Cl/Cl ratios were analyzed by the PRIME Laboratory at Purdue University.

Table 5. Measured ³⁶Cl/Cl ratios for ESF samples, sorted by station

LANL ID	Approx ESF Station	Sampled Feature (from Table 1)	Description of analyzed aliquot	Cl, mg/kg	Br, µg/kg	Br/Cl x 10 ³	Fraction of Cl from construction water (Note A)	³⁶ Cl/Cl ratio (x 10 ⁻¹⁵)			Upper age limit, ky (Note D)
								Measured (Note B)	Corrected (Note C)	% uncert	
E001-1	1+98	Fault zone	Broken bedrock	1.95	554	284	0.09 ± 0.02	516 ± 15	518 ± 17	3	462
E008-2	1+99.8	Fault zone	Gouge	2.61	23	9	0.00 ± 0.00	2132 ± 139	2132 ± 139	7	Bomb
E009-2	1+99.8	Fault zone	Gouge	1.95	15	8	0.00 ± 0.00	2453 ± 169	2452 ± 169	7	Bomb
E010-2	1+99.8	Fault zone	Gouge	2.28	22	9	0.00 ± 0.00	715 ± 49	715 ± 49	7	322
E011-2	1+99.8	Fault zone	Gouge	2.02	19	9	0.00 ± 0.00	2440 ± 159	2440 ± 159	7	Bomb
E012-2	1+99.8	Fault zone	Gouge	2.12	19	9	0.00 ± 0.00	2382 ± 157	2382 ± 157	7	Bomb
E007-2	2+3	Fault zone	Intact bedrock	3.42	221	65	0.02 ± 0.00	519 ± 14	519 ± 14	3	461
E073-1	5+04	Fault?	Breccia/Gouge	5.63	364	65	0.02 ± 0.00	460 ± 14	459 ± 14	3	514
E074-1	5+5.5	Fault?	Breccia/Gouge	11.67	858	74	0.02 ± 0.00	492 ± 17	492 ± 17	4	484
E086-1	11+43	Bedrock	Broken bedrock	0.73	175	241	0.08 ± 0.02	629 ± 19	640 ± 20	3	370
E028-1	12+44	Cooling joints	Broken bedrock	0.25	34	136	0.04 ± 0.01	2560 ± 70	2652 ± 76	3	Bomb
E029-1	13+00	Systematic	Intact bedrock	0.60	10	17	0.00 ± 0.00	628 ± 19	628 ± 19	3	378
E032-2	14+14	Shear zone	Broken bedrock	0.77	35	45	0.01 ± 0.00	663 ± 25	665 ± 25	4	353
E033-1	14+41	Fault	Breccia	0.33	49	147	0.05 ± 0.01	829 ± 39	844 ± 41	5	249
E034-1	15+00	Systematic	Intact bedrock	0.25	36	142	0.04 ± 0.01	937 ± 29	958 ± 30	3	195
E035-1	15+05	Fracture	Breccia	0.97	1376	1420	0.47 ± 0.10	569 ± 19	631 ± 42	7	376

Level 4 Milestone Report 3783AD
March 29, 1996

Table 5. Measured $^{36}\text{Cl}/\text{Cl}$ ratios for ESF samples, sorted by station (continued)

LANL ID	Approx ESF Station	Sampled Feature (from Table 1)	Description of analyzed aliquot	Cl, mg/kg	Br, $\mu\text{g}/\text{kg}$	Br/Cl $\times 10^3$	Fraction of Cl from construction water (Note A)	$^{36}\text{Cl}/\text{Cl}$ ratio ($\times 10^{15}$)			Upper age limit, ky (Note D)
								Measured (Note B)	Corrected (Note C)	% uncert	
E036-1	16+12	Cooling joint	Broken bedrock	1.36	553	407	0.13 ± 0.03	396 ± 31	380 ± 36	9	596
E037-2	16+19	Fracture	Breccia/Gouge	0.51	81	160	0.05 ± 0.01	943 ± 29	967 ± 31	3	191
E038-1	17+00	Systematic	Intact bedrock	0.39	35	88	0.03 ± 0.01	613 ± 124	616 ± 128	21	386
E040-1	18+96	Broken rock	Broken bedrock	0.50	183	365	0.12 ± 0.03	1521 ± 39	1659 ± 53	3	Bomb
E041-1	19+00	Systematic	Intact bedrock	0.63	237	374	0.12 ± 0.03	718 ± 18	748 ± 22	3	302
E042-2	19+31	Breccia	Broken bedrock	0.60	88	148	0.05 ± 0.01	2899 ± 98	3016 ± 106	4	Bomb
E042-3	19+31	Breccia	Broken bedrock	0.61	63	104	0.03 ± 0.01	1795 ± 62	1838 ± 65	4	Bomb
E043-2	19+37	Fault zone	Broken bedrock	0.77	68	88	0.03 ± 0.01	1118 ± 29	1135 ± 30	3	121
E044-2	19+42	Breccia	Broken bedrock	0.56	155	278	0.09 ± 0.02	2120 ± 49	2280 ± 64	3	Bomb
E045-1	21+00	Systematic	Intact bedrock	0.59	137	234	0.08 ± 0.02	763 ± 20	784 ± 22	3	282
E046-1	22+71	Fracture zone	Broken bedrock	0.98	584	599	0.20 ± 0.04	671 ± 15	713 ± 21	3	323
E047-1	23+00	Systematic	Intact bedrock	0.81	84	103	0.03 ± 0.01	639 ± 30	644 ± 31	5	367
E020-1	24+68	Fracture	Broken bedrock	Not yet analyzed			N/A	696 ± 23	695 ± 23	3	334
E051-1	25+00	Systematic	Intact bedrock	0.55	270	487	0.16 ± 0.03	906 ± 28	983 ± 37	4	183
E052-1	26+79	Shear zone	Broken bedrock	0.44	138	313	0.10 ± 0.02	1862 ± 38	2016 ± 54	3	Bomb
E054-1	27+00	Systematic	Intact bedrock	0.42	30	73	0.02 ± 0.00	932 ± 29	941 ± 30	3	202
E058-2	27+66	Fault	Breccia	1.437	22	15	0.00 ± 0.00	459 ± 13	459 ± 13	3	514

Table 5. Measured $^{36}\text{Cl}/\text{Cl}$ ratios for ESF samples, sorted by station (continued)

LANL ID	Approx ESF Station	Sampled Feature (from Table 1)	Description of analyzed aliquot	Cl, mg/kg	Br, $\mu\text{g}/\text{kg}$	Br/Cl $\times 10^3$	Fraction of Cl from construction water (Note A)	$^{36}\text{Cl}/\text{Cl}$ ratio ($\times 10^{-15}$)			Upper age limit, ky (Note D)
								Measured (Note B)	Corrected (Note C)	% uncert	
E059-2	28+40	Fault	Breccia	2.075	128	62	0.02 ± 0.00	516 ± 15	516 ± 15	3	463
E057-2	27+50	Fracture	Breccia	1.3	282	217	0.07 ± 0.01	754 ± 21	773 ± 23	3	288
E141-1	29+00	Systematic	Intact bedrock	0.43	70	163	0.05 ± 0.01	894 ± 32	915 ± 34	4	214
E142-1	29+21	Fracture	Broken bedrock	0.54	455*	849	0.28 ± 0.06	557 ± 15	579 ± 23	4	413
E143-1	29+65	Fault	Broken bedrock	0.43	282*	659	0.22 ± 0.05	932 ± 116	1052 ± 150	14	154
E144-1	29+73	Cooling joint	Broken bedrock	0.22	66	296	0.10 ± 0.02	777 ± 25	806 ± 28	4	270
E147-1	30+27	Cooling joints	Broken bedrock	1.61	549*	341	0.11 ± 0.02	491 ± 11	490 ± 13	3	486
E149-1	31+64	Cooling joint	Broken bedrock	0.71	454	643	0.21 ± 0.05	600 ± 21	627 ± 28	4	379
E150-1	33+00	Systematic	Broken bedrock	0.21	3	16	0.00 ± 0.00	1325 ± 49	1327 ± 49	4	53
E152-1	34+28	Fractures	Broken bedrock	0.26	255	981	0.32 ± 0.07	2806 ± 83	3916 ± 266	7	Bomb
E153-3	34+32	Cooling joints	Broken bedrock	0.23	131	570	0.19 ± 0.04	2710 ± 77	3220 ± 144	4	Bomb
E154-1	34+71	Cooling joints	Breccia	0.33	58	175	0.06 ± 0.01	771 ± 35	787 ± 37	5	280
E154-3	34+71	Cooling joints	Broken bedrock	0.20	36	179	0.06 ± 0.01	3546 ± 74	3730 ± 88	2	Bomb
E155-1	35+00	Systematic	Intact bedrock	0.52	218	416	0.14 ± 0.03	914 ± 44	979 ± 53	5	185
E156-1	35+00	Cooling joints	Broken bedrock	1.00	297	297	0.10 ± 0.02	605 ± 24	616 ± 27	4	386
E158-1	35+08	Cooling joints	Breccia	0.73	666	912	0.30 ± 0.06	914 ± 21	1093 ± 49	5	137
E158-3	35+08	Cooling joints	Broken bedrock	0.46	468*	1021	0.34 ± 0.07	1924 ± 64	2652 ± 183	7	Bomb

Level 4 Milestone Report 3783AD
March 29, 1996

Table 5. Measured $^{36}\text{Cl}/\text{Cl}$ ratios for ESF samples, sorted by station (continued)

LANL ID	Approx ESF Station	Sampled Feature (from Table 1)	Description of analyzed aliquot	Cl, mg/kg	Br, $\mu\text{g}/\text{kg}$	Br/Cl $\times 10^3$	Fraction of Cl from construction water (Note A)	$^{36}\text{Cl}/\text{Cl}$ ratio ($\times 10^{-15}$)			Upper age limit, ky (Note D)
								Measured (Note B)	Corrected (Note C)	% uncert	
E160-1	35+45	Fracture	Broken bedrock	0.25	201	802	0.27 ± 0.06	2703 ± 54	3498 ± 185	5	Bomb
E161-3	35+58	Cooling joint	Broken bedrock	0.54	266*	493	0.16 ± 0.03	1872 ± 32	2137 ± 68	3	Bomb

Notes:

- * Preliminary results only; Br concentrations are to be reanalyzed for these samples.
- A. Estimated using equation (1) in the text, assuming a Br/Cl ratio of 3 for construction water and 0.009 for meteoric water.
- B. $^{36}\text{Cl}/\text{Cl}$ ratios were analyzed by the PRIME Laboratory at Purdue University. Measured ratios have been adjusted for the addition of tracer but not for the effects of dilution by construction water or rock Cl.
- C. Corrected for dilution by construction water using equation (2) in the text assuming that construction water has a $^{36}\text{Cl}/\text{Cl}$ ratio of 500×10^{-15} . Uncertainty estimate includes analytical error and assumes 20% uncertainty in construction water Br/Cl. Samples for which the final corrected $^{36}\text{Cl}/\text{Cl}$ ratio has an associated uncertainty exceeding 25% have been excluded from this table.
- D. Upper age limit assuming a maximum initial meteoric $^{36}\text{Cl}/\text{Cl}$ ratio of 1500×10^{-15} . The ^{36}Cl signal is interpreted as bomb-pulse for $^{36}\text{Cl}/\text{Cl}$ ratios exceeding 1500×10^{-15} .

Table 6. Correction of measured $^{36}\text{Cl}/\text{Cl}$ ratios for dilution by rock chloride, for ream-cutting samples from borehole UE-25 UZ#16

LANL ID	Strat. unit (Note A)	Ave. depth (m)	Measured values (Note B)		Case 1 (Note C) (Soil Br/Cl)		Case 2 (Note C) (Rain Br/Cl)	
			$^{36}\text{Cl}/\text{Cl} \times 10^{-15}$	$\text{Br}/\text{Cl} \times 10^{-3}$	Meteoric fraction of Cl	Corrected $^{36}\text{Cl}/\text{Cl} \times 10^{-15}$	Meteoric fraction of Cl	Corrected $^{36}\text{Cl}/\text{Cl} \times 10^{-15}$
R179	TCw	22	74.5	2.0	0.07	761	0.02	2200
R180	TCw	38	108	2.1	0.10	941	0.03	2728
R182	PTn	44	106	3.3	0.36	259	0.12	722
R183	PTn	47	346	10.4	*	346	0.66	515
R184	PTn	48	329	15.7	*	329	*	329
R185	PTn	50	338	16.6	*	338	*	338
R186	PTn	55	306	11.2	*	306	0.71	421
R187	PTn	67	434	10.8	*	434	0.68	626
R205	TSw	204	145	3.8	0.47	286	0.16	801
R206	TSw	216	351	9.1	1.64	222	0.56	615
R210	TSw	255	192	5.7	0.89	213	0.30	587
R214	TSw	290	275	4.3	0.58	459	0.20	1311
R216	TSw	307	116	3.1	0.32	322	0.11	907
R218	TSw	317	177	3.3	0.36	456	0.12	1302
R219	TSw	332	123	3.9	0.49	231	0.17	642
R220	TSw	339	117	3.3	0.36	289	0.12	812
R221	TSw	342	150	5.4	0.82	178	0.28	484
R224	CHn	356	272	5.0	0.74	363	0.25	1028
R225	CHn	357	363	9.4	*	363	0.58	611
R376	CHn	395	508	8.3	*	508	0.50	1001

Table 6. (continued)

LANL ID	Strat. unit (Note A)	Ave. depth (m)	Measured values (Note B)		Case 1 (Note C) (Soil Br/Cl)		Case 2 (Note C) (Rain Br/Cl)	
			$^{36}\text{Cl}/\text{Cl} \times 10^{-15}$	$\text{Br}/\text{Cl} \times 10^{-3}$	Meteoric fraction of Cl	Corrected $^{36}\text{Cl}/\text{Cl} \times 10^{-15}$	Meteoric fraction of Cl	Corrected $^{36}\text{Cl}/\text{Cl} \times 10^{-15}$
R383	CHn	426	616	9.8	*	616	0.61	997
R387	CHn	437	620	9.0	*	620	0.55	1111
R388	CHn	440	648	9.4	*	648	0.58	1103
R392	PP	453	354	6.2	1.00	354	0.34	1002
R394	PP	463	327	5.7	0.89	365	0.30	1035
R398	PP	481	266	6.2	1.00	266	0.34	744
R400	PP	483	320	5.7	0.89	357	0.30	1012
R401	PP	488	231	5.0	0.74	307	0.25	864
R402	PP	490	105	2.1	0.10	909	0.03	2636
R403	PP	492	251	3.7	0.45	535	0.15	1535
R404	PP	493	265	3.7	0.45	566	0.15	1627
R405	PP	494	274	4.6	0.65	413	0.22	1175

Notes:

- A. Stratigraphic units: TCw, Tiva Canyon welded; PTn, Paintbrush nonwelded; TSw, Topopah Spring welded; CHn, Calico Hills nonwelded; PP, Prow Pass
- B. Measured values reported in Fabryka-Martin and Liu (in prep.) and in YMP notebooks cited in Acknowledgments.
- C. Assumptions about end-member Br/Cl ratios:
 - ▶ For Case 1, the meteoric Br/Cl is assumed to be 0.0062, as measured for alluvium and deep soil (Fabryka-Martin and Liu, in prep.).
 - ▶ For Case 2, the meteoric Br/Cl is assumed to be 0.015, as measured for rainwater (Fabryka-Martin and Liu, in prep.).
 - ▶ For both cases, the rock Br/Cl ratio is set at a value of 0.00167, based on step-leaching experiments (Fabryka-Martin and Liu, in prep.).
- * For cases in which the measured Br/Cl ratio exceeds the value of the meteoric end-member, it is assumed that the measured $^{36}\text{Cl}/\text{Cl}$ ratio requires no correction for rock Cl.

Table 7. Correction of measured $^{36}\text{Cl}/\text{Cl}$ ratios for dilution by rock chloride, for ream-cutting samples from borehole USW UZ-14

LANL ID	Strat. unit (Note A)	Ave. depth (m)	Measured values (Note B)		Case 1 (Note C) (Soil Br/Cl)		Case 2 (Note C) (Rain Br/Cl)	
			$^{36}\text{Cl}/\text{Cl} \times 10^{-15}$	Br/Cl $\times 10^{-3}$	Meteoric fraction of Cl	Corrected $^{36}\text{Cl}/\text{Cl} \times 10^{-15}$	Meteoric fraction of Cl	Corrected $^{36}\text{Cl}/\text{Cl} \times 10^{-15}$
R419	PTn	81	440	3.2	0.34	1262	0.11	3672
R420	PTn	84	457	4.6	0.65	695	0.22	2006
R421	PTn/TSw	86	202	4.9	0.71	275	0.24	771
R422	TSw	88	112	3.8	0.47	216	0.16	595
R423	TSw	383	165	4.6	0.65	244	0.22	679
R424	TSw	393	265	5.4	0.82	318	0.28	895
R427	TSw	397	300	4.1	0.54	537	0.18	1542
R428	TSw/CHn	427	443	7.6	*	443	0.44	971

Notes:

- A. Stratigraphic units: TCw, Tiva Canyon welded; PTn, Paintbrush nonwelded; TSw, Topopah Spring welded; CHn, Calico Hills nonwelded; PP, Prow Pass
 - B. Measured values reported in Fabryka-Martin and Liu (in prep.) and in YMP notebooks cited in Acknowledgments.
 - C. Assumptions about end-member Br/Cl ratios:
 - ▶ For Case 1, the meteoric Br/Cl is assumed to be 0.0062, as measured for alluvium and deep soil (Fabryka-Martin and Liu, in prep.).
 - ▶ For Case 2, the meteoric Br/Cl is assumed to be 0.015, as measured for rainwater (Fabryka-Martin and Liu, in prep.).
 - ▶ For both cases, the rock Br/Cl ratio is set at a value of 0.00167, based on step-leaching experiments (Fabryka-Martin and Liu, in prep.).
- * For cases in which the measured Br/Cl ratio exceeds the value of the meteoric end-member, it is assumed that the measured $^{36}\text{Cl}/\text{Cl}$ ratio requires no correction for rock Cl.

Table 8. PTn fracture parameters for FEHM simulations

CASE	Fracture Aperture (m)	Fracture Density (m ⁻¹)	Fracture Permeability k _f (m ²)	Matrix Block Length Scale L _f (m)	Fracture Porosity φ _f	van Genuchten Parameters	
						α _f (m ⁻¹)	n _f
Base	3.5 x 10 ⁻⁴	0.6	1.0 x 10 ⁻⁸	0.83	9.27 x 10 ⁻³	10.0	3.0
A	3.5 x 10 ⁻⁴	1.2	1.0 x 10 ⁻⁸	0.41	1.85 x 10 ⁻⁴	10.0	3.0
B	6.9 x 10 ⁻⁴	0.6	4.0 x 10 ⁻⁸	0.83	1.85 x 10 ⁻⁴	20.0	3.0
C	6.9 x 10 ⁻⁴	1.2	4.0 x 10 ⁻⁸	0.41	3.70 x 10 ⁻⁴	20.0	3.0
D	3.5 x 10 ⁻⁴	0.6	1.0 x 10 ⁻⁸	0.83	9.27 x 10 ⁻³	1.0	3.0
E	6.9 x 10 ⁻⁴	1.2	4.0 x 10 ⁻⁸	0.41	3.70 x 10 ⁻⁴	1.0	3.0

Table 9. Travel-time estimates (years) from FEHM simulations (see note)

Infiltration Rate:		0.1 mm/yr		1 mm/yr		5 mm/yr		10 mm/yr		50 mm/yr	
Flow Fraction:		matrix	fracture	matrix	fracture	matrix	fracture	matrix	fracture	matrix	fracture
Case		99%	1%	24%	76%	6%	94%	3%	97%	0.6%	99.4%
Case	Arrival										
Base	Bomb Pulse?	No	No	No	No	No	No	No	No	No	No
	1%	280800	130200	48400	11800	30800	2500	27800	1200	23600	200
	5%	281900	204600	51000	17600	31300	2500	28000	1300	23700	200
	50%	281900	210300	54500	22100	32700	4500	28700	2300	23900	300
A	Bomb Pulse?					No	No	No	No		
	1%					31000	2500	27800	1300		
	5%					31400	2500	28000	1300		
	50%					32600	4500	28700	2300		
B	Bomb Pulse?			No	No	No	Yes				
	1%			48400	12100	30500	2200				
	5%			51200	17800	31200	2600				
	50%			54500	22300	32400	4600				
C	Bomb Pulse?			No	No	No	No	No	Yes		
	1%			48900	12000	30900	2400	27800	1100		
	5%			51200	17800	31300	2500	28000	1300		
	50%			54500	21800	32400	4100	28700	2300		
D	Bomb Pulse?			No	No	No	Yes				
	1%			47300	11500	30600	2300				
	5%			49400	16500	31200	2500				
	50%			53400	21600	32400	4500				
E	Bomb Pulse?			No	Yes	No	Yes				
	1%			41900	10700	29300	1100				
	5%			48900	14800	30200	2000				
	50%			53900	21200	32400	4600				

Note: For each combination of parameter set and infiltration rate, travel times between the ground surface and the ESF are calculated separately for water arriving at the ESF in matrix and in fractures. The travel time distribution is presented in terms of the 1st, 5th, and 50th percentiles. An additional "bomb pulse" notation indicates whether any water arrives within 50 years. For example, for case A with 5 mm/yr infiltration, no water arrives through the matrix within 50 years, 1% of the matrix water is younger than 31,000 years, 5% is younger than 31,400 years, and 50% is younger than 32,600 years. A double-lined box indicates that a particular combination of parameters would predict a component of bomb-pulse ³⁶Cl to be present in the fracture fluid reaching the ESF.

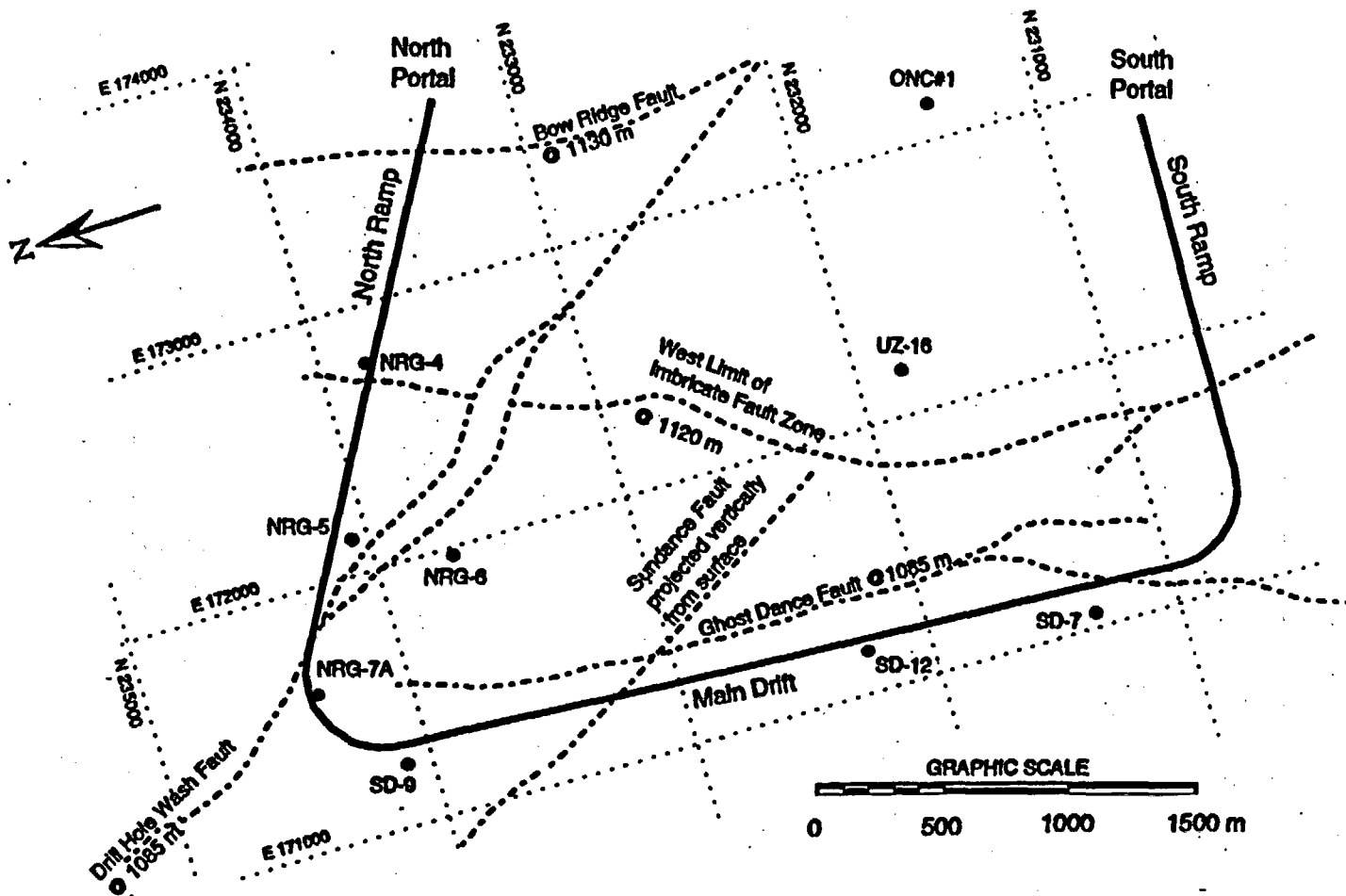


Figure 1. Schematic plan view of ESF North Ramp, Main Drift, and South Ramp projections, showing locations of major faults and nearby boreholes (based on LA-EES-13-LV-03-96-001, Attachment 4) for which samples exist for ^{36}Cl analysis. Fault traces are approximations and may differ from their true locations, particularly at the level of the ESF. ESF coordinates may differ from final as-built coordinates.

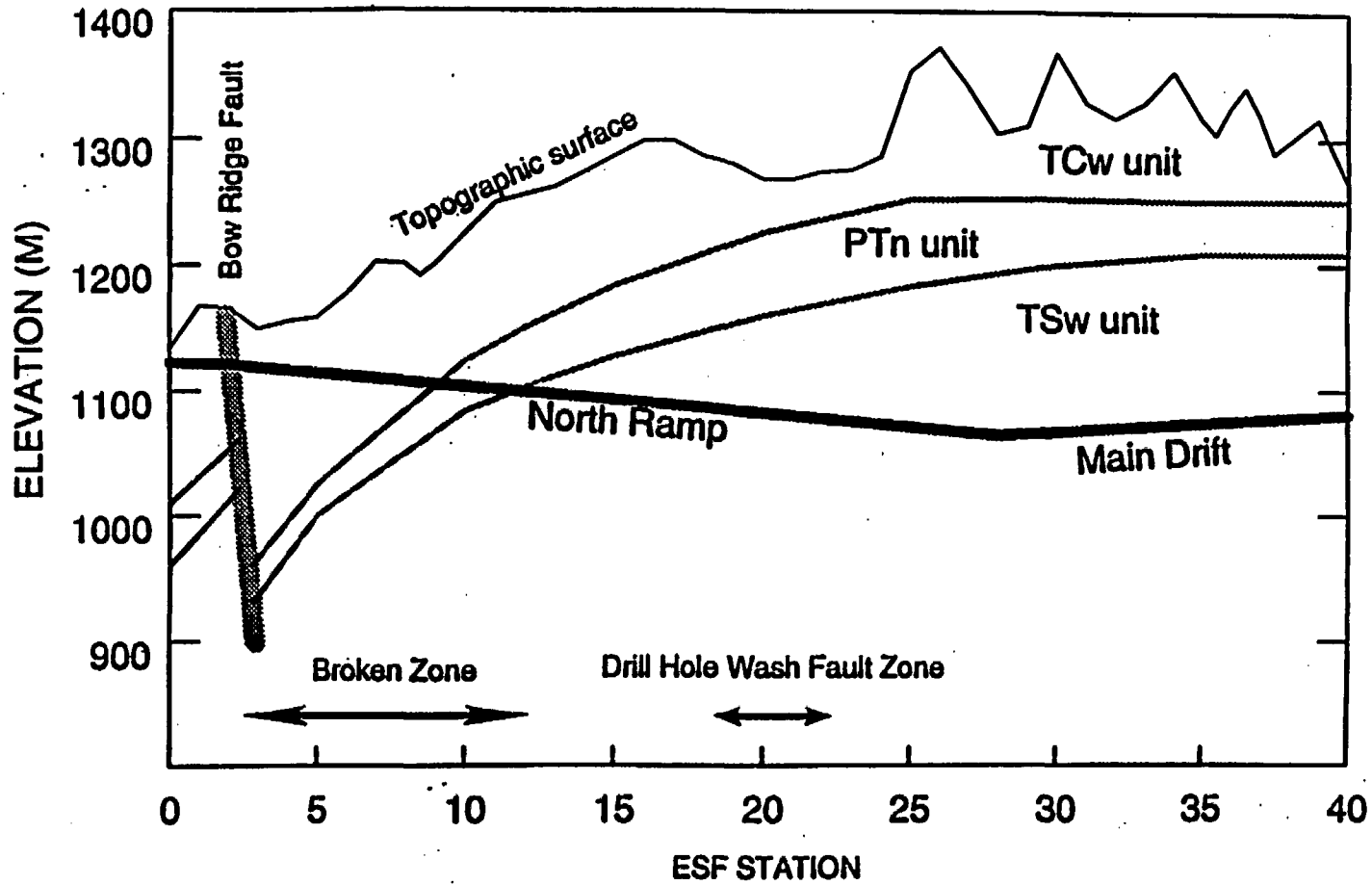


Figure 2. Schematic cross-section of ESF tunnel, showing approximate locations of the surface, major stratigraphic units, and major structural features as a function of distance along the North Ramp and Main Drift. ESF stations are marked in units of 100 m. The North Ramp extends from Station 0 to 28, and the Main Drift starts at Station 28. See Figure 1 for a plan view of the ESF tunnel.

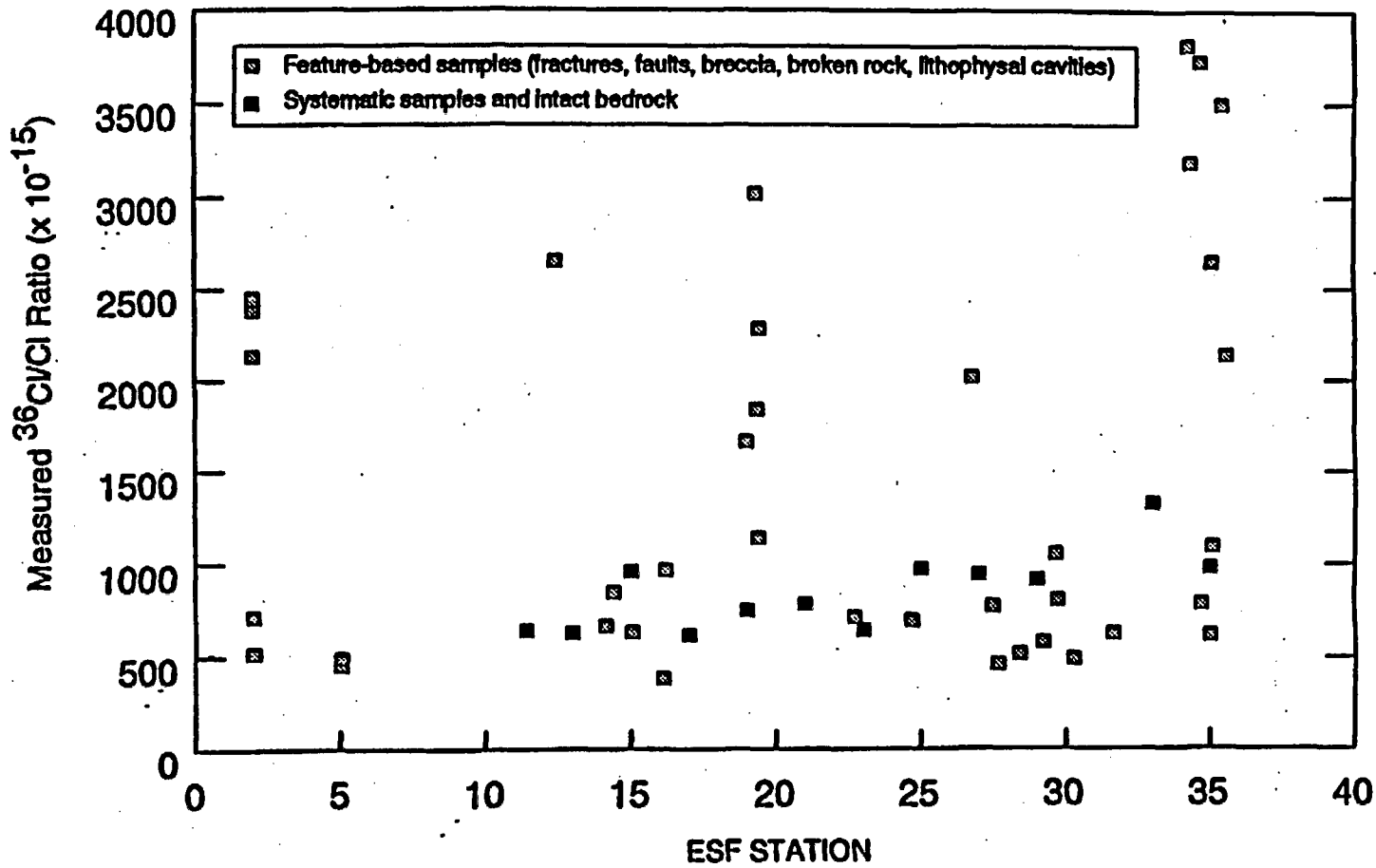


Figure 3. Distribution of $^{36}\text{Cl}/\text{Cl}$ ratios measured for rock samples, as a function of distance along the ESF North Ramp and Main Drift. ESF stations are marked in 100-m increments. Samples with ratios exceeding $1500 (\times 10^{-15})$ are considered to contain a component of bomb-pulse ^{36}Cl . Data from Table 5.

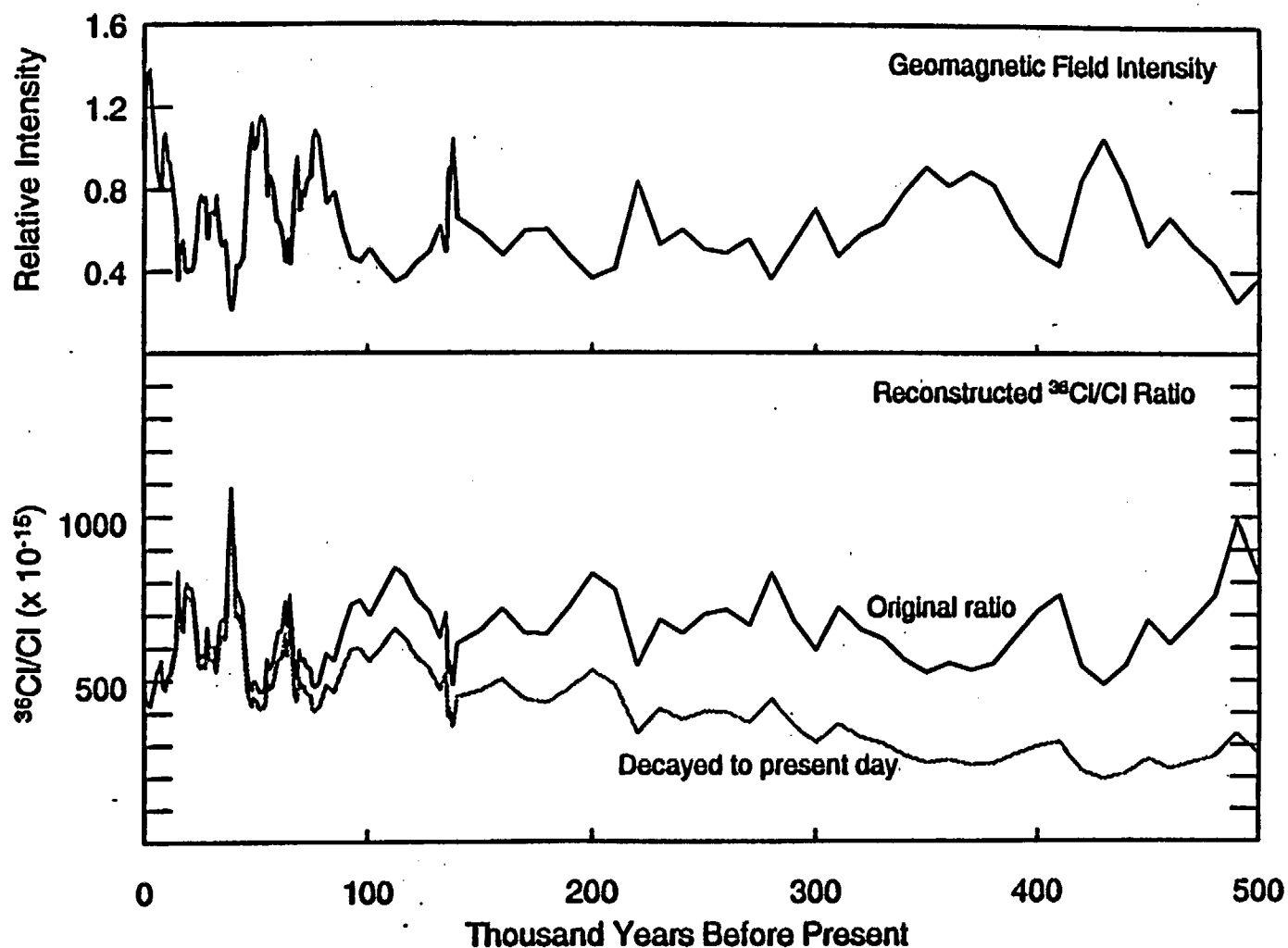


Figure 4. Variations in geomagnetic field intensity and corresponding theoretical production of chlorine-36 in the atmosphere. Reconstructed $^{36}\text{Cl}/\text{Cl}$ ratios assume a constant deposition rate equivalent to that of the present day at Yucca Mountain. Higher or lower deposition rates would lead to correspondingly lower or higher ratios, respectively. Note that this model indicates that the atmospheric $^{36}\text{Cl}/\text{Cl}$ signal has been elevated well above 500 ($\times 10^{-15}$) for at least the past 500 ky.

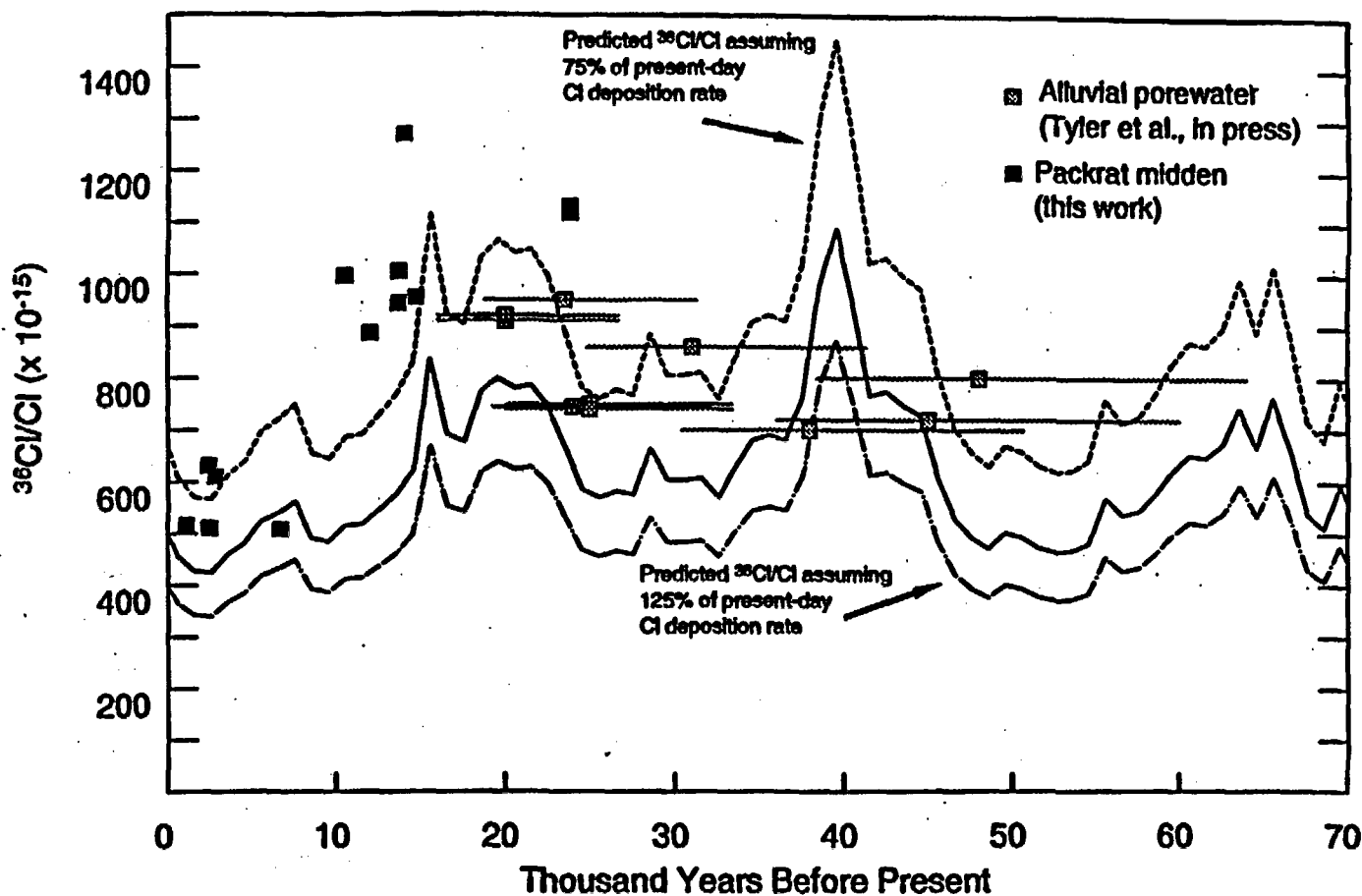


Figure 5. Predicted variations in production of chlorine-36 in the atmosphere, compared against measured data for packrat middens [present work] and alluvial porewaters [Tyler et al., in press] from the vicinity of the Nevada Test Site. Lower and upper limits shown for the reconstructed $^{36}\text{Cl}/\text{Cl}$ ratios assume that the stable chloride deposition rate may have been 25% greater or lesser than that of the present day, respectively. Ranges in the alluvial porewater ages are established based on these same ranges for the accumulation rate of chloride in the alluvial profiles. Note that both the model as well as the data indicate that the atmospheric $^{36}\text{Cl}/\text{Cl}$ signal has been elevated well above $500 (x 10^{-15})$ for at least the time period shown.

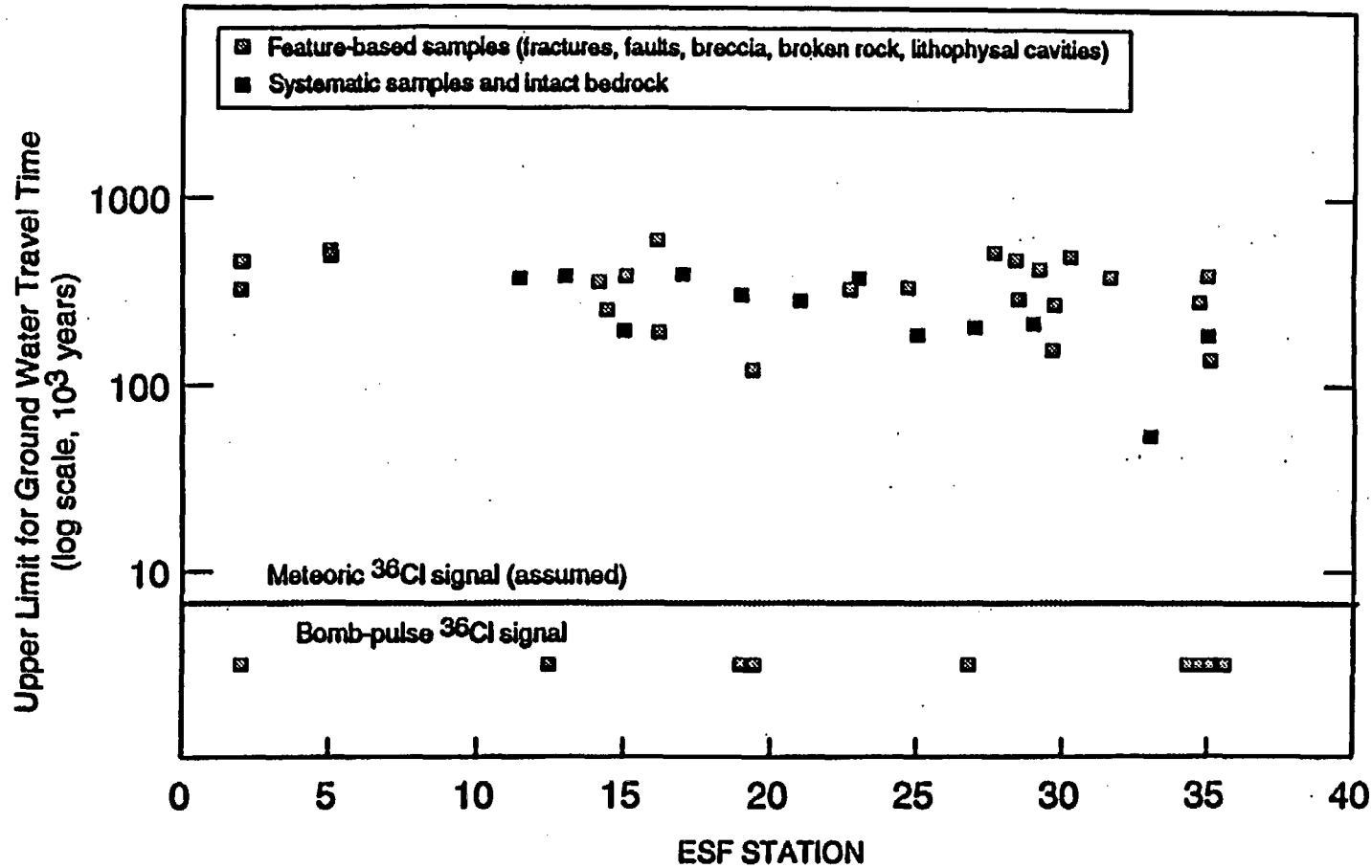


Figure 6. Upper limits for ground water travel times as a function of distance along the ESF North Ramp and Main Drift. Travel times are based on radioactive decay of the ³⁶Cl signal measured in ESF rock samples, assuming an initial ³⁶Cl/Cl ratio of 1500 (x 10⁻¹⁵). Samples with ratios exceeding 1500 (x 10⁻¹⁵) are considered to contain a component of bomb-pulse ³⁶Cl. Data from Table 5.

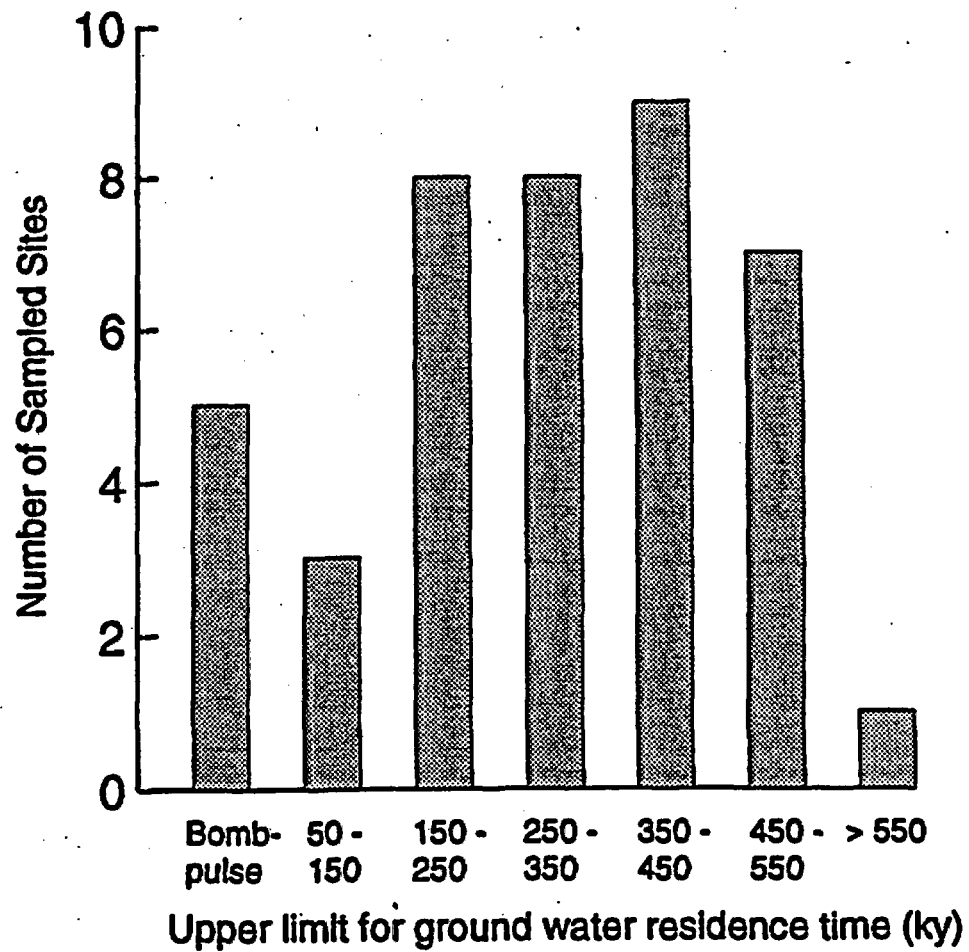


Figure 7. Frequency distribution of upper limits for ground water travel times in the ESF, assuming a maximum initial meteoric $^{36}\text{C}/\text{Cl}$ ratio of $1500 (x 10^{-16})$. Five sites are indicated as containing a bomb-pulse signal, based on clustering of results evident in Figure 6.

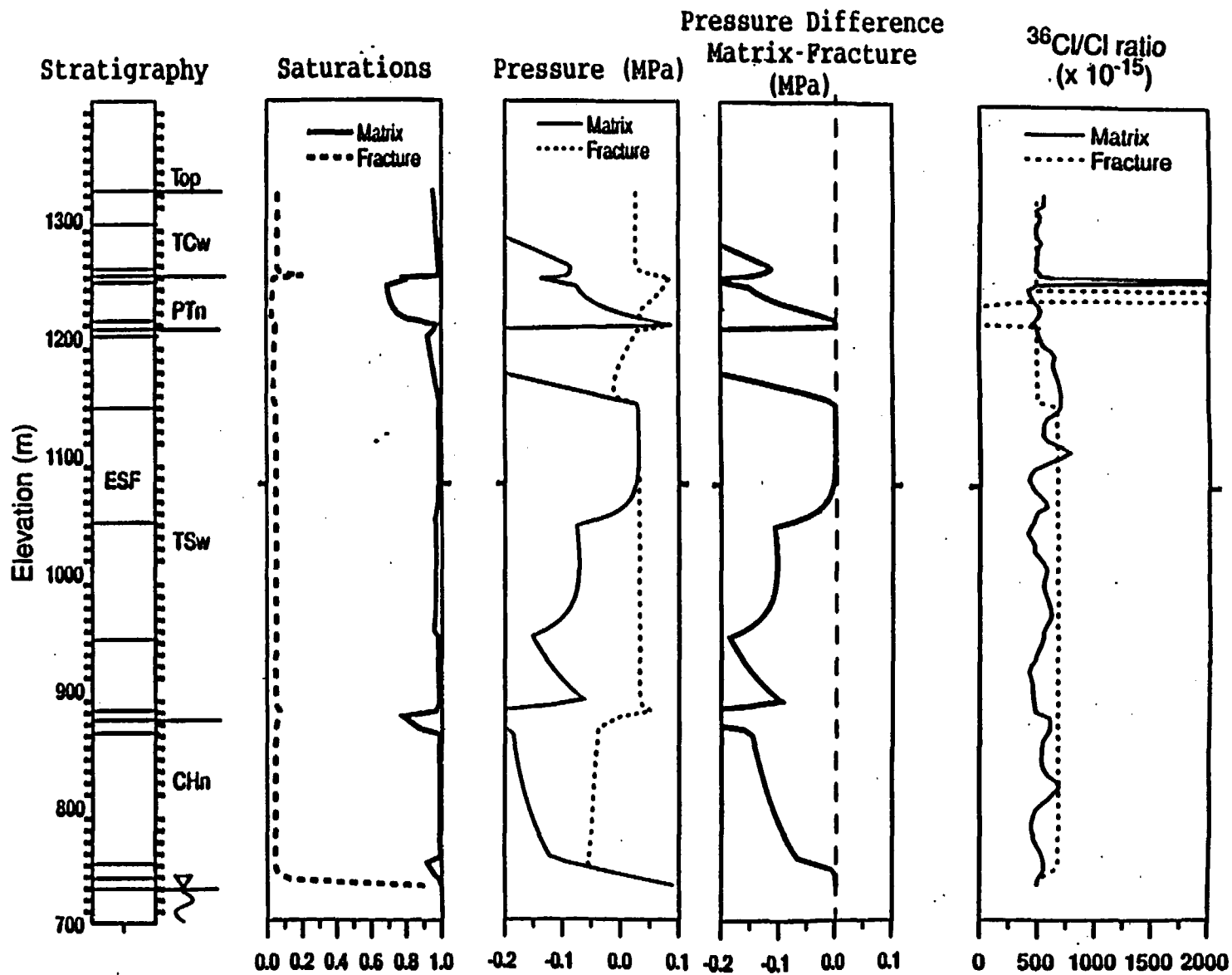


Figure 8. Station 35 description and model results for base-case properties and 1 mm/yr infiltration rate.

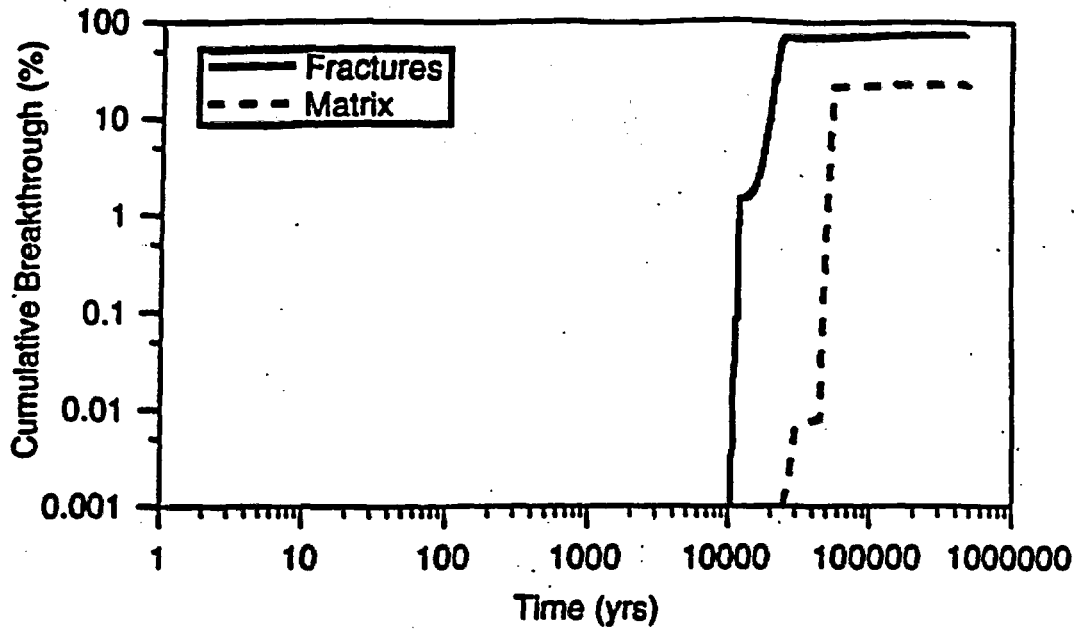


Figure 9. Cumulative breakthrough for 1.0 mm/yr infiltration rate and base-case properties.

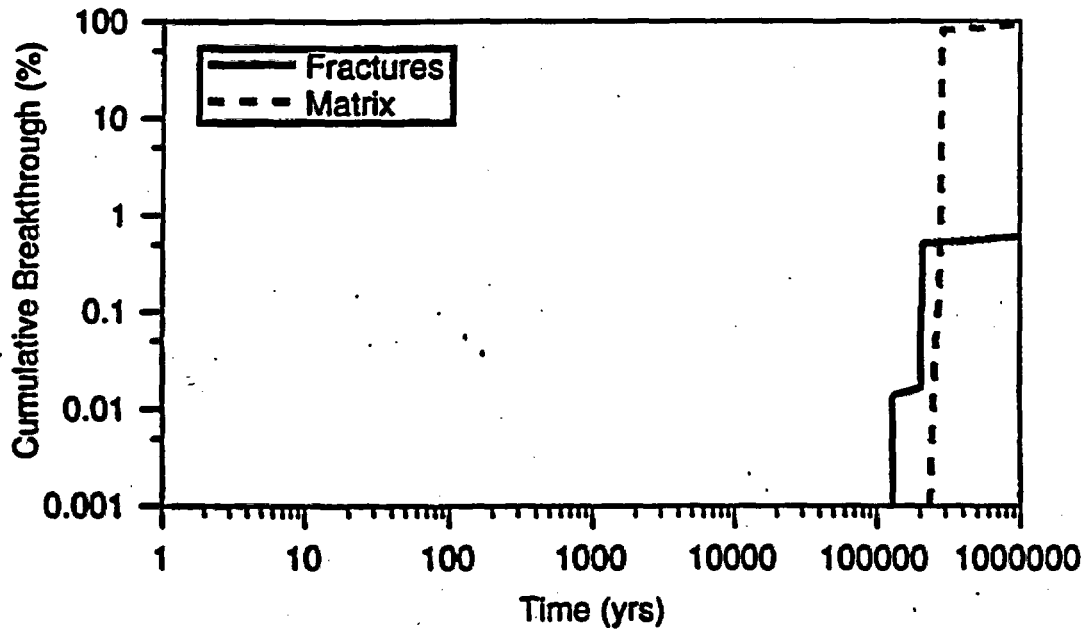


Figure 10. Cumulative breakthrough for 0.1 mm/yr infiltration rate and base-case properties

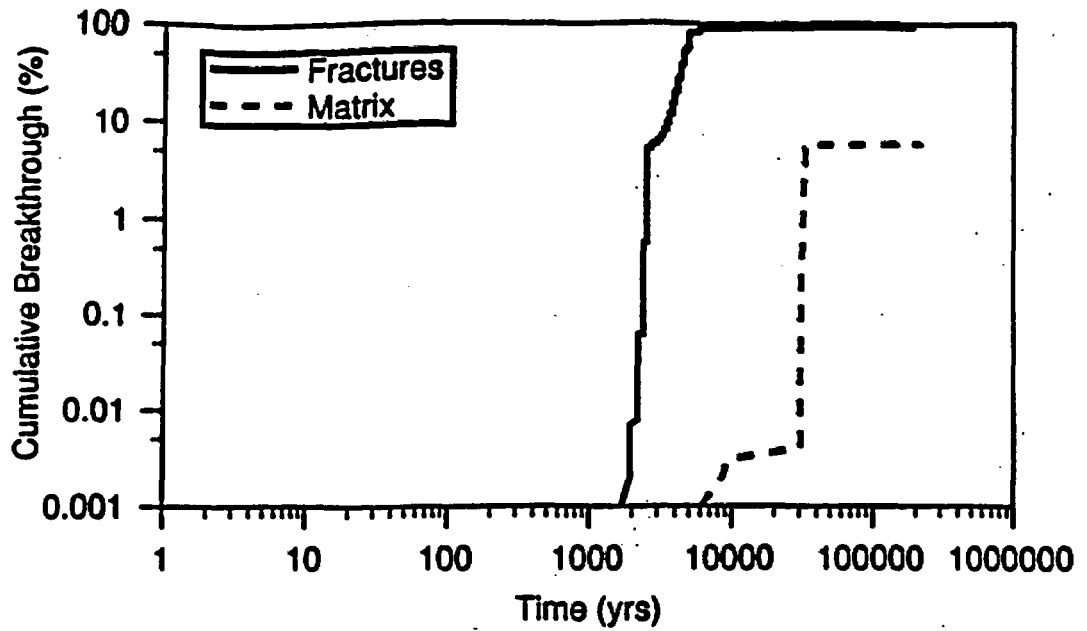


Figure 11. Cumulative breakthrough for 5.0 mm/yr infiltration rate and base-case properties.

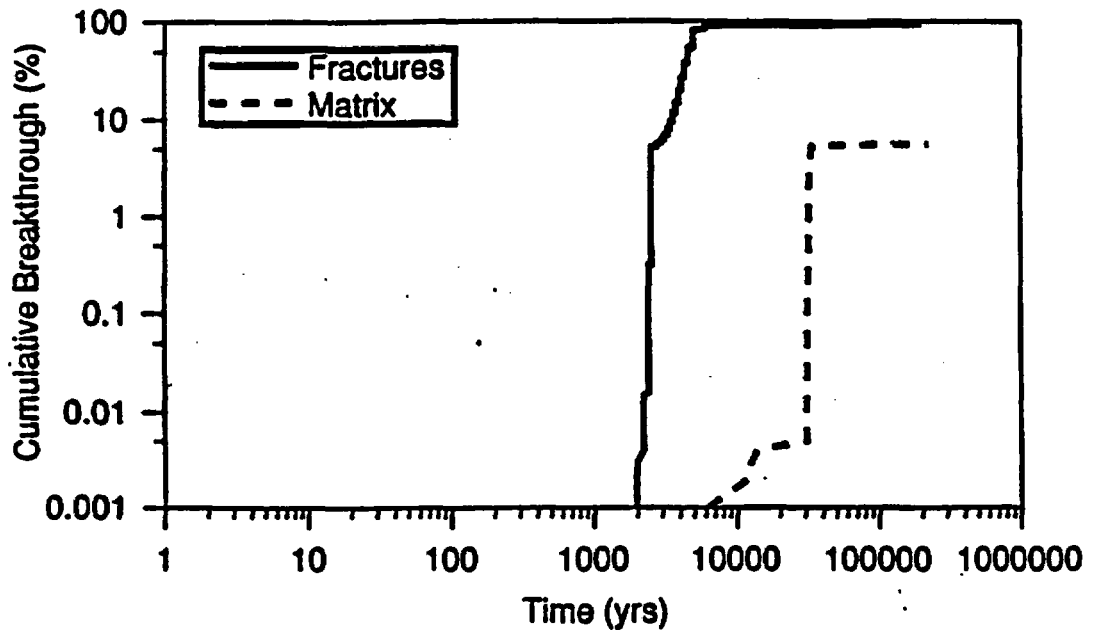


Figure 12. Cumulative breakthrough for 5.0 mm/yr infiltration rate and Case A properties.

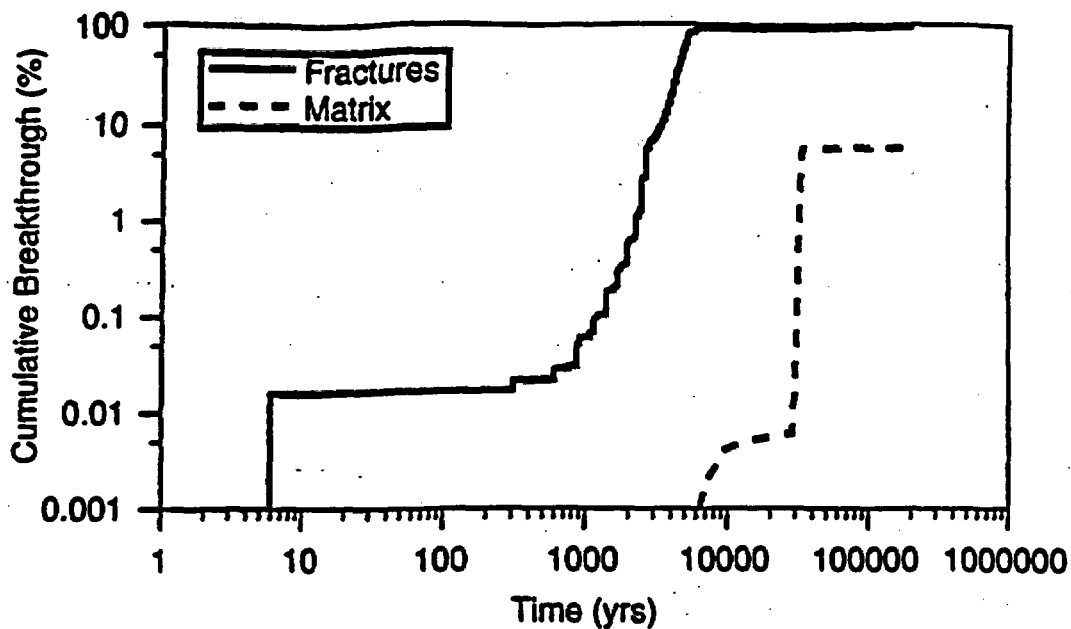


Figure 13. Cumulative breakthrough for 5.0 mm/yr infiltration rate and Case B properties.

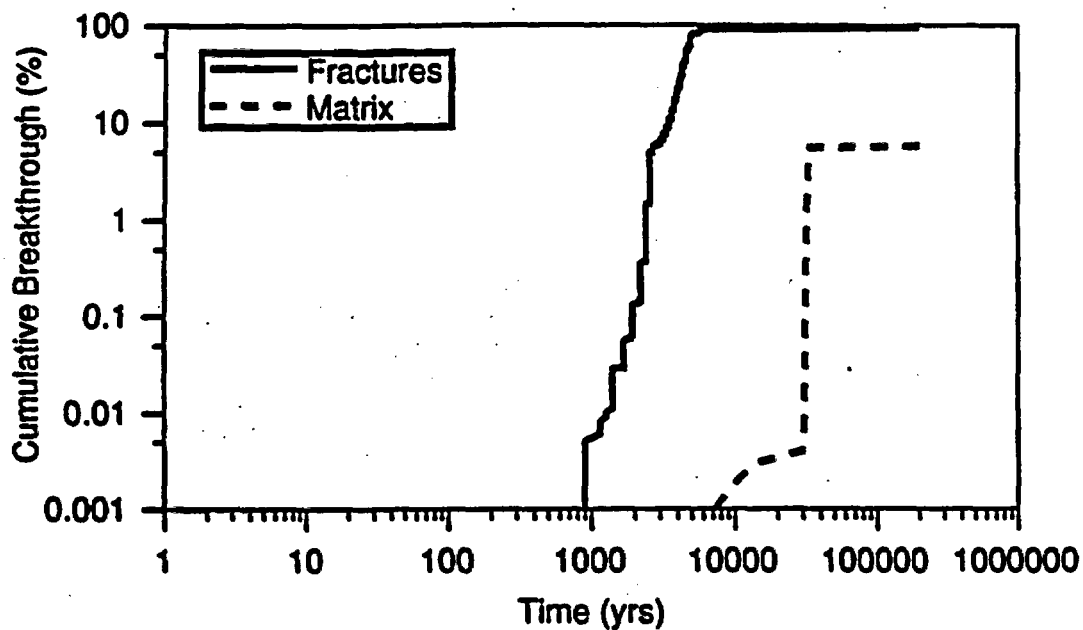


Figure 14. Cumulative breakthrough for 5.0 mm/yr infiltration rate and Case C properties.

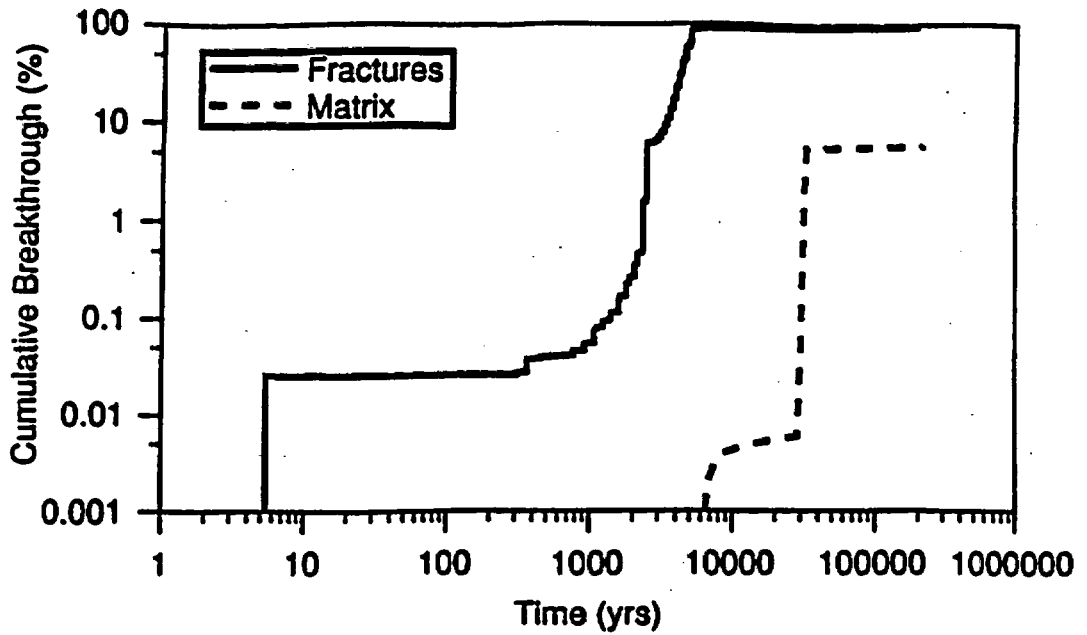


Figure 15. Cumulative breakthrough for 5.0 mm/yr infiltration rate and Case D properties.

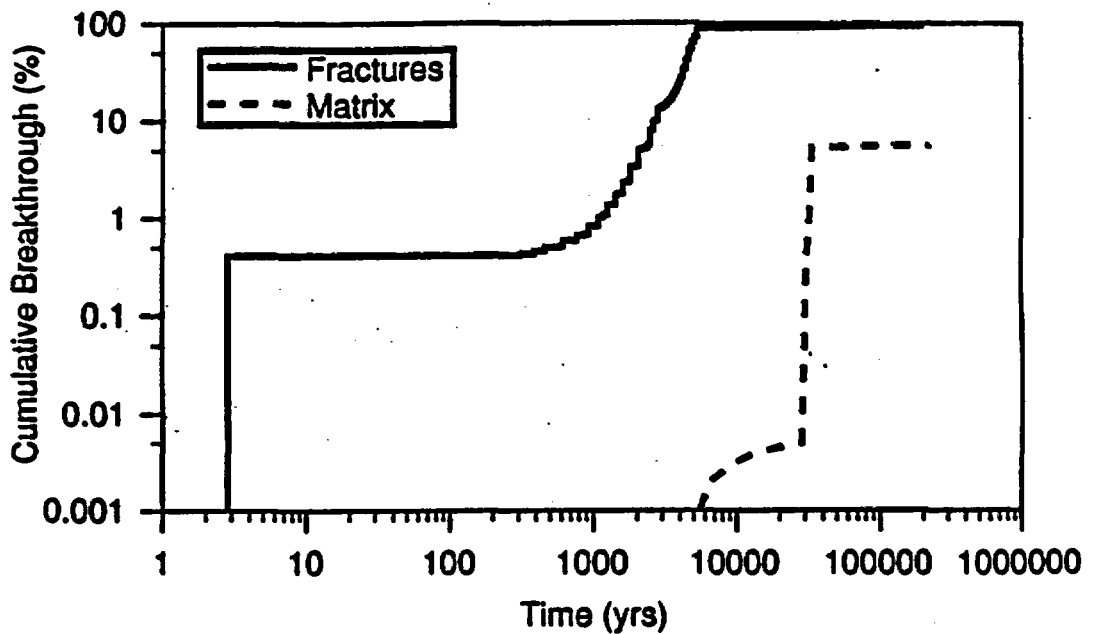


Figure 16. Cumulative breakthrough for 5.0 mm/yr infiltration rate and Case E properties

APPENDIX A

SITE AND SAMPLE DESCRIPTIONS

The purpose of these descriptions is to document the nature of the bedrock, the presence of field-scale structures such as faults, fractures, breccia zones, and other features that affect rock permeability, and the existence of secondary mineral deposits indicating that water has moved through the rocks. The descriptive process is in progress and many of the descriptions remain to be done or are incomplete, lacking either site or sample information. All of the sample sites for which descriptions are included here were chosen for the existence of a possible flow path, water-laid mineral deposit, or representative bedrock.

As described in Section 3, particular attention has been devoted to features with implications for continuity of flow paths. In the context of Yucca Mountain geology, the term "syngenetic" refers to features that formed during the deposition or cooling of a pyroclastic unit. Syngenetic features such as cooling joints and some fracture zones could serve as fluid conduits, but do not normally extend beyond the boundaries of the host unit. For example, a cooling joint in the Topopah Spring Tuff with geochemical evidence of recent flow must have received its fluid input from a different conductive feature in the overlying nonwelded tuff. In contrast, a fault with evidence of repeated movement could by itself be a direct flow path from the surface to the Topopah Spring Tuff.

E001 (Sta 1+98)

The bedrock is densely welded, devitrified lithophysal Tiva Canyon Tuff from the eastern wall of the Bow Ridge fault zone. The Bow Ridge fault is a westward-dipping normal fault with displacement downward to the west. The rock is fractured and fragmental. Individual fragments are more than 2 cm across, very irregular due to the lithophysae, and mostly angular to subangular.

The rock contains about 10% lithophysal cavities up to 3 cm across. The cavities have bleached borders up to 1 cm thick. Vapor-phase minerals in the cavities are feldspar, crystalline silica, and Fe-Ti oxides, all less than 1 mm. There may be some clay as well. Less than 5% of the cavities contain sprays of weakly UV-fluorescent drusy quartz overlying the vapor-phase minerals. Rock surfaces have less than 1% coverage of dendritic to diffuse spots of manganese minerals and a more widespread overcoating of powdery white material. The existence of these coatings suggests that the bedrock is highly fractured even beyond the boundary of the fault zone.

E007 (Sta 2+3)

This bedrock sample is medium-grained nonwelded pre-Rainier Mesa tuff from the downthrown western wall of the Bow Ridge fault. There is no evidence of fracturing or fracture-filling minerals.

The original glassy components of the rock have been completely replaced by zeolites, probably clinoptilolite. The pyroclastic constituents included about 30 to 50% of mostly white pumice clasts less than 1 cm across, 10 to 20% dark lithic grains less than 3 mm across, less than 5% phenocrysts of mostly feldspar and lesser bleached biotite, and the remainder of fine ash. No calcite or UV-fluorescent silica is present.

E008 (Sta 1+99.8)

This sample was collected from within the Bow Ridge fault zone which is several meters wide at the ESF tunnel level. The fault gouge is composed of fragments of densely welded, devitrified Tiva Canyon Tuff. Individual breccia clasts range from more than 5 cm across to less than 150 μm . There are local segregations of the fine-grained material. Larger clasts are somewhat rounded.

Some of the larger clasts have dendritic coatings of manganese minerals. All clasts are coated with a less than 1 mm thick powdery white layer composed of feldspar, smectite, quartz, tridymite, cristobalite, calcite, and hematite, in order of decreasing abundance. Most of this may be material of vapor-phase and lower-temperature hydrothermal origin redistributed onto the surfaces of the breccia clasts. There is local tight cementation of the fine-grained breccia and adjacent coarser clasts by less than 1 mm thick coatings of less than 0.2 mm calcite crystals whose overall abundance is undetermined. The calcite is also covered with white powder. No UV-fluorescent or otherwise visually identifiable silica is present.

E010 (Sta 1+99.8)

This sample from the Bow Ridge fault zone consists of ~2- to 5-cm rubble. The rubble clasts are subangular to subrounded and are either intact densely welded, devitrified Tiva Canyon bedrock or loosely cemented Tiva Canyon breccia, in about equal proportions. The brecciated tuff consists of ≤ 1 -cm fragments of fractured tuff cemented by gray-white, slightly clayey, $\ll 1$ -mm material. Rubble clasts of intact rock commonly have ≤ 1 mm-thick coatings of powdery gray-white material.

Most rock fragments have scattered surficial patches of dendritic manganese minerals. On newly broken breccia clast fracture surfaces, a few of the manganese patches surround highly weathered mafic minerals. No calcite or UV-fluorescent silica was observed.

E011 (Sta 1+99.8)

This sample consists of mostly coarse (>1 cm) rubble and minor fine-grained breccia from the Bow Ridge fault zone. The rubble clasts are all densely welded, devitrified Tiva Canyon Tuff and are mostly subequant and subangular.

About 95% of the brecciated rock surfaces are coated with a <1 mm-thick layer of pale pink to buff powdery material. In a few places where the coating is thin or absent, discontinuous coatings of dendritic manganese minerals cover less than 5% of the rock surfaces. In the fine-grained breccia and on a few coarse clast surfaces, there are <<1 mm-thick coatings of <0.5 mm calcite crystals with probably rhombohedral morphology. Most of the calcite shows little fluorescence, except for a few 1 to 2 mm wide patches that fluoresce white (more strongly in long- than in short-wave UV-light). Some calcite may have a very thin, visually undetectable, coating of opal because it shows weak yellow-green fluorescence in short-wave UV light. The calcite does not form a dense cement, and there are small cavities <1 mm within the fine-grained breccia that lack calcite or powdery coatings.

E020 (Sta 24+68)

The sample site is a partly syngenetic rubbly breccia in sparsely lithophysal densely welded, devitrified Topopah Spring Tuff. Individual breccia clasts, up to at least 10 cm across, are coated on most surfaces with vapor-phase feldspar and silica. Feldspar is more common in the lithophysae and silica is more common on the fracture surfaces. The lithophysae are up to 2 cm across, with bleached borders.

The clasts have less than 1% coverage of surface-conformal crusts less than 1 mm thick of semi-aligned quartz crystals. There are also isolated patches of <1 mm drusy quartz crystals and associated rare botryoids of silica with granular surfaces (probable opal-CT). None of this silica is UV-fluorescent. All of this silica is partly overgrown by calcite. The calcite, in <1 mm equant crystals or <1 cm blades, fills some lithophysae (blades) and covers broken rock surfaces with or without underlying vapor-phase coatings (equant and blades). UV-fluorescent opal, in not quite clear <1 mm botryoids, are locally associated with calcite and have an overall abundance of 1 to 2%. The opal exists as overgrowths and intergrowths or inclusions in calcite. There are also <1 mm spheres of powdery white, possibly fluorescent silica preserved only as inclusions in calcite.

E028 (Sta 12+44)

The host bedrock is densely welded, devitrified, nonlithophysal, crystal-rich Topopah Spring Tuff. The sampled structure is a set of two near-vertical cooling cracks 30 cm to 1 m apart, with the intervening rock cut by a second set of sub-horizontal cooling cracks perpendicular to the main fractures. This feature is traceable from invert to crown on both ribs of the tunnel. Similar features are spaced laterally about 10 to 20 m apart.

The sampled rock contains about 10-15% phenocrysts of mostly alkali feldspar. Pumice lapilli constitute about 10% and commonly contain vapor-phase alteration cavities up to 2 cm across. The main secondary mineral in the vapor-phase cavities is clear to white crystalline silica. The prominent cooling cracks have widespread but incomplete coatings, less than 1 mm thick, of mostly white, granular to arborescent, non-UV-fluorescent silica, probably a vapor-phase product. Some cooling cracks and other, more irregular cracks, have 1 to 2 mm thick veneers of

less than 1 mm tuff detritus cemented in place by UV-fluorescent botryoidal silica, mostly blue-gray and slightly translucent. Locally, the botryoidal texture grades into surface-conformal aggregates of subparallel 1 to 2 mm drusy quartz crystals. This cement locally overlies the vapor-phase silica. Isolated aggregates of drusy quartz are perched along fractures, especially fracture intersections. The dominant botryoidal silica cement also contains some white and nearly opaque silica. A small amount of clear sub-botryoidal opal overlies the rest of the silica cement, especially in depressions. No calcite was observed.

E030 (Sta 13+67)

The sampled material is rubble composed of subangular to subrounded clasts of densely welded, devitrified crystal-rich Topopah Spring Tuff. The rock is slightly crumbly due to pervasive vapor-phase alteration of the pumice lapilli to feldspar, crystalline silica, and Fe-Ti oxides. The surfaces of some of the larger rubble clasts exhibit domains of <1 mm rock fragments cemented by vapor-phase minerals, and some areas of the rubble surfaces have coatings of vapor-phase minerals extending beyond the boundaries of altered pumices. These textural relations suggest that brecciation was at least partly syngenetic. No calcite or UV-fluorescent silica was observed.

E035 (Sta 15+05)

The sampled rock is a calcite-cemented, mostly syngenetic breccia of densely welded, devitrified Topopah Spring Tuff. The maximum clast size is about 2 cm. Most fragments are coated with <1 mm vapor phase minerals, mostly feldspar, silica, and minor Fe-Ti oxides. Slightly disaggregated vapor-phase minerals also serve as breccia matrix. A few clasts may have smectite-zeolite-silica alteration. A newly separated fracture surface shows the clay-rich clasts and pink-gray clay fracture coatings.

The breccia is tightly cemented by poikilitic calcite that comprises about 30% of the rock. In rare cavities within the cement, <1 mm across, the calcite has flat rhombohedral terminations. A prominent irregular fracture surface has a 0 to 2 mm-thick coating of flat rhombohedral calcite crystals <2 mm across. Overlying this calcite are <1 mm spots of silica that are mostly whitish, waxy, and subopaque, rarely clear. The silica, with an overall abundance on the fracture surface of <2%, fluoresces green in short-wave UV light. There are very rare manganese mineral coatings, mostly on tuff fragments, but also possibly on adjacent calcite crystals.

E036 (Sta 16+12)

This sample is a separated cooling joint in densely welded, devitrified Topopah Spring Tuff, with calcite infilling. Vapor-phase cavities in pumice lapilli are coated with feldspar, silica, and Fe-Ti oxides. Most cavities have infillings of calcite over the vapor-phase minerals.

The separated cooling joint was initially filled with botryoidal chalcedony overlain by drusy quartz. The chalcedony and quartz separated from the joint wall and the intervening space was

almost completely filled with dense mosaic calcite consisting of <1 mm crystals with flat rhombohedral terminations on free surfaces. The calcite shows faint laminations parallel to the joint surface, especially under short-wave UV light, perhaps related to variable content of very-fine-grained tuffaceous impurities. The laminations may indicate progressive opening and infilling of the joint. There are also calcite overgrowths on the drusy quartz away from the joint surface. Rare pale yellow <1 mm aggregates of silica occur with calcite in the interstices of the drusy quartz crystals. The surfaces of the mosaic calcite deposits are locally covered with thin patches 1 to 3 mm across of water-clear botryoidal silica with blocky surfaces, probably opal-CT. An unidentified rose-lavender very fine-grained mineral on fractured surfaces of the mosaic calcite is rare but locally prominent.

E040 (Sta 18+96)

The bedrock at the sampling site is lithophysal, densely welded, devitrified Topopah Spring Tuff. The lithophysal cavities are up to 0.5 m wide, and lithophysal fractures with vapor-phase mineral coatings are common. The rock is cut by many short-segment (<1 m), high-angle cooling cracks. Small amounts of calcite are present in the exposed rock, but not in the sampled material.

Rock fragments in the sampled material are mostly 5 to 10 cm across, angular, and equant to elongate. The smaller lithophysal cavities and partings, coated with vapor-phase minerals, are elongate parallel to the rock layering caused by flow and welding. The vapor-phase altered borders on the cavities and partings are up to about 1 cm thick. The <1 mm crystals lining the cavities and partings are feldspar, crystalline silica, and minor Fe-Ti oxides. Away from the central lithophysal cavities, the vapor-phase crystals are finer grained, <0.1 mm. Most rock fragment surfaces, especially those that are smoother and more planar (probable cooling cracks), have <<1 mm translucent to transparent coatings of probable cryptocrystalline silica. Locally, the silica has an equally thin overcoat of pale blue-gray clay. There is a dusting of loose to somewhat adhesive vapor-phase material on all rock surfaces. No calcite or UV-fluorescent silica was observed in the sampled material.

E042 (Sta 19+31)

The sampled bedrock is lithophysal, densely welded, devitrified Topopah Spring Tuff. The abundant lithophysal cavities are less than 20 cm across. The rock is generally broken into mostly <10 cm fragments. Orientation and extent of the broken rock zone are unknown. There are no obvious throughgoing fractures, but a possible adjacent fracture zone parallel to the tunnel axis may have been mostly removed during mining. Calcite fillings in a cluster of lithophysal cavities about 1 m above and to the right of the collection site suggests a possible flow pathway.

There is preferential breakage and comminution of the vapor-phase altered margins of lithophysal cavities and vapor-phase altered pumice lapilli. This soft material is composed of <0.1 mm crystals of feldspar and crystalline silica. Networks of fine (<<1 mm apertures) fractures within the breccia clasts are filled with poikilitic calcite, and the surfaces of the clasts

have <1 mm-thick coatings of poikilitic calcite with a variety of surface terminations. The pore spaces between the larger clasts, i.e., larger than a few millimeters, are not completely filled with calcite although the surface coatings are sufficient to form a tight cement. The calcite is not UV-fluorescent, and no fluorescent silica was observed.

E044 (Sta 19+42)

The sample site is a crackle breccia zone in lithophysal, densely welded, devitrified Topopah Spring Tuff. The breccia zone is about 3 m wide and laterally bounded by discrete fractures. The breccia is fairly tight, with little or no realignment of the blocks. The breccia zone extends from the invert about halfway up the right rib, but the opposite rib shows more upward continuity.

Lithophysal cavities are up to about 3 cm across and lined with <1 mm crystals of feldspar, silica, and Fe-Ti oxides. The angular fragments are locally coated with <<1 mm crystals of vapor-phase minerals, suggesting that the fragmentation of the rock is at least partly syngenetic. A ubiquitous white powder on the rock surfaces contains vapor-phase minerals that may have been redistributed from lithophysae. UV-fluorescent calcite cement is widespread but not abundant. Coatings of <1 mm calcite crystals are located in some lithophysal cavities and adjacent surfaces of intersecting fractures. No UV-fluorescent silica was detected in the sample.

E046 (Sta 22+71)

The site is a near-vertical fracture zone about 6 m wide that extends about 2/3 of the distance from the invert to the crown. The bedrock is lithophysal, densely welded, devitrified Topopah Spring Tuff. Lithophysal cavities, mostly <30 cm, comprise about 40% of the rock, and there are numerous lithophysal fractures. Some of the fractures have calcite coatings, but no calcite was observed in the lithophysae.

The lithophysal cavities and fractures are commonly coated by <1 mm vapor-phase crystals of feldspar and Fe-Ti oxides. The highly irregular surfaces of the lithophysal fractures are also variably coated with at least three varieties of silica, as well as calcite. The least abundant variety is a combination of clear botryoidal and irregular lacy masses of UV-fluorescent opal. This material is overlain by drusy quartz crystals in a dense coating or open network, about 1 mm thick. Some quartz lies directly on the rock surface on or the vapor-phase feldspar. Some crystals are skeletal or hollow or form surface-conformal crusts, up to several cm across, of semi-aligned crystals with prism faces parallel to the rock surface. Examples exist in which the outer margins of quartz crusts are nonfluorescent and have a fairly sharp boundary with the fluorescent quartz, although no obvious morphological boundary is visible.

Sparry calcite forms <1 mm-thick, discontinuous coatings on the quartz, especially filling the interstices of the network and the centers of hollow crystals. A minor amount of calcite also

occurs as film-like crystal aggregates directly on the rock surface. Domains of fine-grained bedrock breccia, cemented by calcite and possibly by quartz, also exist.

E050 (Sta 24+40)

The sampled material is fault gouge and calcite from a near-vertical fault following an old cooling crack in lithophysal, densely welded, devitrified Topopah Spring Tuff. Some large lithophysal cavities are intersected by the fault trace, and many have calcite overlying the ≥ 1 cm-thick vapor-phase mineral coatings.

The gouge itself, as sampled, is uncemented and contains no detectable UV-fluorescent silica. A local deposit of calcite, separated for $^{36}\text{Cl}/\text{Cl}$ analysis, was the only calcite observed within the fault. Centimeter-scale clasts are subangular to subrounded and have scattered thin coatings of vapor-phase minerals, mostly feldspar and crystalline silica, typical of the smaller lithophysal cavities. Most clasts, including those < 1 mm, are coated with light buff powdery material.

E052 (Sta 26+79)

The bedrock is densely welded, devitrified Topopah Spring Tuff with $> 10\%$ lithophysal cavities up to 0.5 m across. Some cavities are aligned parallel to adjacent or intersecting fractures, some of which are cooling cracks. The sampling site includes a near-vertical, probable cooling crack with multiple traces within a 1 m-wide zone, traceable about $3/4$ of the distance from invert to crown. Fracture apertures are generally ≤ 1 mm. Fractures like this occur at about a 3- to 4-m spacing along the tunnel wall. There are no obvious coatings of calcite or manganese minerals on the fracture walls, but most of the larger lithophysae have 2- to 3-cm-thick crusts of 1 to 2 mm calcite crystals on the bottoms and sides of the cavities.

Smaller lithophysal cavities, a few centimeters across, have < 1 mm-thick coatings of < 1 mm crystals of feldspar, crystalline silica, and Fe-Ti oxides. Examination of one cooling crack surface revealed scattered 1 to 2-mm patches of very thin and very fine-grained blue-gray silica. None of the silica fluoresces in UV light. No calcite was observed in the small cavities or on the fracture surface.

E146 (Sta 30+18)

The analyzed mineral separate is from a lithophysal-devitrification cavity about 1 m across in densely welded, devitrified Topopah Spring Tuff with $< 5\%$ lithophysae in an area of few throughgoing fractures. The cavity is intersected by at least one cooling crack with smooth surfaces and bleached margins.

Resting on the bottom of the cavity are loose crusts of platy, pearly calcite aggregates up to ~ 2 cm thick. There are many local textural varieties of calcite. Common forms, all less than 1 mm long, include steep rhombohedra grouped on the surfaces of larger crystals, tapering hairlike

crystals, and beadlike strings of crystals. Many of these forms have textural features suggestive of both deposition and dissolution. In some places, extremely thin, ribbonlike calcite aggregates have grown as much as several centimeters upward from the crystalline crusts.

Clear opal-A occurs locally with calcite as intergrowths and, more abundantly, as thin overgrowths. Both the calcite and the opal fluoresce in short-wave UV light.